Check for updates

RESEARCH ARTICLE

NANO · MICRO small
www.small-journal.com

Battery-Free, Wireless Multi-Modal Sensor, and Actuator Array System for Pressure Injury Prevention

Hyeonseok Han, Hyunwoo Park, Seokjoo Cho, Sung-Uk Lee, Jungrak Choi, Ji-Hwan Ha, Jaeho Park, Young Jung, Hyunjin Kim, Junseong Ahn, Yeong Jae Kwon, Yong Suk Oh, Minkyu Je,* and Inkyu Park**

Simultaneous monitoring of critical parameters (e.g., pressure, shear, and temperature) at bony prominences is essential for the prevention of pressure injuries in a systematic manner. However, the development of wireless sensor array for accurate mapping of risk factors has been limited due to the challenges in the convergence of wireless technologies and wearable sensor arrays with a thin and small form factor. Herein, a battery-free, wireless, miniaturized multi-modal sensor array is introduced for continuous mapping of pressure, shear, and temperature at skin interfaces. The sensor array includes an integrated pressure and shear sensor consisting of 3D strain gauges and micromachined components. The mechanically decoupled design of the integrated sensor enables reliable data acquisition of pressure and shear at skin interfaces without the need for additional data processing. The sensor platform enables the analysis of interplay among localized pressure, shear, and temperature in response to changes in the patient's movement, posture, and bed inclination. The validation trials using a novel combination of wireless sensor arrays and customized pneumatic actuator demonstrate the efficacy of the platform in continuous monitoring and efficient redistribution of pressure and shear without repositioning, thereby improving the patient's quality of life.

1. Introduction

Pressure and shear applied to the skin interface over bony prominences leads to deformation of underlying tissue, which results in the occlusion of blood perfusion on the arterial side (i.e., ischemia) and, then, reduces oxygen and nutrients supply to the tissue.[1–8] This reduction in oxygen and nutrient supply contributes to the development of tissue necrosis (i.e., pressure injuries). In addition, pressure injuries deteriorate with elevated body temperature due to a concomitant increase in the tissue metabolism of 10%/°C requiring oxygen consumption in the lesion.[9] A convergence of risk factors including pressure, shear, temperature, and other variables exacerbates the development of pressure injuries.[10] Patients with pressure injuries endure severe pain, reduced functionality, decreased mobility, and an increased risk of serious complications such as cellulitis and osteomyelitis, leading to a significant deterioration in the quality of life. Pressure injury is a frequently occurring damage, with a reported high prevalence rate ranging from 14% to 42% in hospitalized patients.[10] In the United States, more than 2.5 million patients suffer from pressure injuries, which contributes to an estimated cost of $9 to $11 billion and 60 000 deaths each year.[11] For the prevention of pressure injuries, turning the body position of patient (i.e., repositioning) to relieve prolonged pressure at critical sites is a fundamental intervention.[12]

H. Han, S. Cho, J.-H. Ha, J. Park, H. Kim, Y. J. Kwon, I. Park
Department of Mechanical Engineering
Korea Advanced Institute of Science and Technology
Daejeon 34141, Republic of Korea
E-mail: inkyu@kaist.ac.kr

H. Park, M. Je
School of Electrical Engineering
Korea Advanced Institute of Science and Technology
Daejeon 34141, Republic of Korea
E-mail: mkje@kaist.ac.kr

S.-U. Lee
Advanced 3D Printing Technology Development Division
Korea Atomic Energy Research Institute
Daejeon 34057, Republic of Korea

The ORCID identification number(s) for the author(s) of this article can be found under https://doi.org/10.1002/smll.202405493

DOI: 10.1002/smll.202405493

J. Choi
Electronics and Telecommunications Research Institute (ETRI)
Daejeon 34129, Republic of Korea

Y. Jung
Department of Mechanical Engineering
Pukyong National University
Busan 48513, Republic of Korea

J. Ahn
Department of Electro-Mechanical Systems Engineering
Korea University
Sejong 30019, Republic of Korea

Y. S. Oh
Department of Mechanical Engineering
Changwon National University
Changwon 51140, Republic of Korea
E-mail: oyongsuk@changwon.ac.kr

 © 2024 Wiley-VCH GmbH

Wireless, wearable multi-modal sensors have been developed to continuously monitor risk factors (e.g., pressure and/or temperature) for the prevention or treatment of ulcers at skin interfaces.[13–21] However, the previous wireless sensors have been equipped with a single Micro Controller Unit (MCU) to support one sensing device (i.e., one sensor device per MCU), which measures pressure and/or temperature, but not shear.[13–21] Besides, array configurations consisting of unit sensors attached to curved surfaces can capture more accurate and reliable mapping data (e.g., mismatch in the effective area) compared to a single sensor with limited spatial densities,[22–24] but the development of wireless sensor array for measurement of risk factors at skin interfaces has been limited due to the challenges in the convergence of wireless technologies and wearable sensor arrays with a thin and small form factor. In addition, despite the significance of measuring pressure and shear (i.e., resultant forces) at skin interfaces as a primary variable in the prevention of pressure injuries,[1–8,25] the development of sensors capable of measuring resultant forces has also been impeded due to the difficulty of mechanically decoupling normal and shear forces in a way that satisfies small form factor of the sensor (i.e., complex and bulky structures).[26–28] In other words, previous sensors that measure resultant forces are mainly mechanically coupled (Table S1, Supporting Information),[27,29–32] and not properly packaged, resulting in poor durability. Above all, mechanically coupled sensors using soft elastomeric materials not only require additional data processing to separate resultant forces into pressure and shear, but also generate nonlinearity and hysteresis in the sensor signal under multi-axial deformation. Therefore, accurate and simultaneous measurement of pressure, shear, and temperature yields invaluable insights for the prevention of pressure injuries, based on quantitative analysis of variables associated with ulcer formation. However, researches on the simultaneous measurement of pressure, shear, and temperature at the interface between the skin and the mattress has not yet been introduced.

In this paper, we report a battery-free, wireless multi-modal sensor array for continuous measurement of pressure, shear, and temperature at skin interfaces. Regarding miniaturized sensing elements, the design includes 3D strain gauges, micromachined components within the shear sensor, and rigid components to achieve mechanical decoupling of normal and shear forces, as well as mechanical durability. Near Field Communication (NFC) platform in wireless technology supports the development of wireless, wearable sensor with a thin and small form factor for biomedical applications.[13,17,19–22] The thin and small form factor is an essential design consideration because medical device-related pressure injuries can be developed at the skin interfaces when using conventional wired and bulky medical devices.[33,34] To enhance the existing NFC platform,[19,20,22] we integrated an NFC SoC with a multiplexer (MUX) and a low-dropout (LDO) regulator with miniaturized sensor devices that have a small and thin form factor. This modification aimed at the development of a wireless sensor array that can support eight sensor devices with a single MCU (i.e., eight sensor devices per MCU) using MUX for improved spatial densities of sensor array and stabilize antenna rectified voltage of NFC SoC using LDO, respectively. Validation trials using a novel combination of wireless sensor arrays and a customized pneumatic actuator presented significant potential in tracking critical sites to monitor and relieve applied pressure and shear at skin interfaces for the prevention of pressure injuries with a minimal workforce of medical staff.

2. Results

2.1. Overall System and a Battery-Free, Wireless Sensor Array

Figure 1a presents schematic illustrations of the overall system that includes 1) battery-free, wireless sensor arrays attached to bony prominences, 2) a wireless platform (two primary antennas), 3) a pneumatic actuator integrated with a clinical bed, and 4) a laptop for real-time monitoring and actuation. Receiver antennas of two sensor arrays, located on the sacrum (4 × 4 array; highlighted in red) and ischium (3 × 3 array; highlighted in yellow), wirelessly interact with two primary antennas (ID ANT800/600, Feig Electronic, Germany) on the clinical bed for power transfer and data communication through Near Field Communication (NFC) at a resonant frequency of 13.56 MHz. The laptop sequentially collects data transmitted from the receiver antennas of sensor arrays to the primary antenna through a multiplexer module (ID ANT.MUX.M4, Feig Electronic, Germany) and an antenna reader (ID LRM2500, Feig Electronics, Germany), as well as displays mapping information of pressure, shear and temperature in real-time. Based on the mapping data of pressure and shear obtained from the wireless sensing platform, pneumatic actuator can be controlled to either inflate or deflate air cells through control software. This actuation aims to reduce pressure and shear values at skin interfaces without intervention of manual handling by caregivers or nurses.

Schematic illustrations in Figure 1b,c present exploded views of 4 × 4 array (highlighted in red) and 3 × 3 array (highlighted in yellow) for measurement of pressure, shear, and temperature at skin interfaces. 4 × 4 array includes 16 pressure sensors and 2 temperature sensors for monitoring across large interfaces (65 × 65 mm^2) of the human body. In addition, the 3 × 3 array includes 9 pressure sensors, 1 shear sensor, and 2 temperature sensors for monitoring pressure, shear, and temperature simultaneously. Figure 1d,e shows the photographs of 4 × 4 array (highlighted in red) and 3 × 3 arrays (highlighted in yellow) before encapsulation, respectively. For application to curved skin interfaces such as elbow and heel (i.e., bony prominences), additional two types of hexagonal arrays with edge lengths of 16 and 40 mm were designed for conformal attachment to curved surfaces in Figure S1 (See Note S1, Supporting Information for the rationale for design considerations of sensor arrays attached to various skin interfaces).

Figure 1f presents photographs of miniaturized pressure (left; 4 × 4 × 1.1 mm^3) and shear (right; 4 × 4 × 1.2 mm^3) sensors. In terms of form factor, the sensors are eight times smaller compared to previously proposed sensors (Figrue S2, Supporting Information),[19,20,22] providing a basis for accurate measurement of pressure and shear at skin interfaces.[14] Figure S3 (Supporting Information) presents the experimental setup used to evaluate the effect of form factor on the sensor response under the identical pressure. The experiment was conducted using two pressure sensors of different sizes (8 × 8 × 2 mm^3 and 4 × 4 × 1.1 mm^3) that shows an eightfold difference in form factor, tested on two types of surfaces (i.e., rigid mattress and soft memory foam). Interestingly, on a hard surface (mattress), the signal

© 2024 Wiley-VCH GmbH

16136829, 2024, 50, Downloaded from https://onlinelibrary.wiley.com/doi/10.1002/smll.202405493 by Korea University Medical Library, Wiley Online Library on [23/12/2024]. See the Terms and Conditions (https://onlinelibrary.wiley.com/terms-and-conditions) on Wiley Online Library for rules of use; OA articles are governed by the applicable Creative Commons License

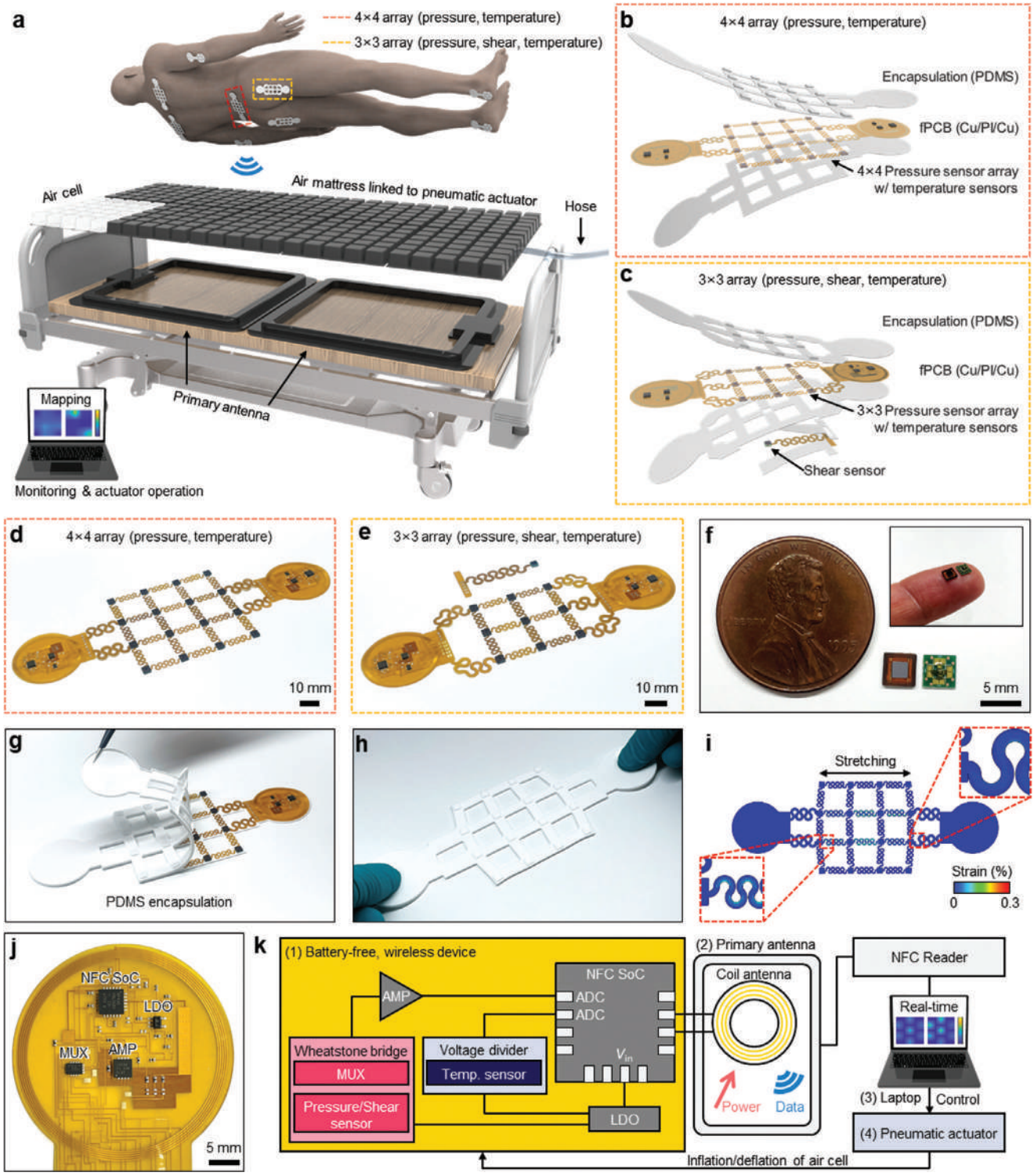


Figure 1. Schematic illustrations and images for a battery-free, wireless sensor array and pneumatic actuator. a) Schematic illustration of the overall system consisting of sensor array on bony prominences, wireless platform, and pneumatic actuator integrated with clinical bed. Exploded view of b) 4 × 4 sensor array and c) 3 × 3 sensor array for measurement of pressure, shear, and temperature at skin interfaces. Photographs of d) 4 × 4 sensor array and e) 3 × 3 sensor array without encapsulation. f) photograph of unit sensors; left, pressure and temperature sensors; right, shear sensor; Photographs of g) 4 × 4 sensor array before PDMS encapsulation, h) 4 × 4 sensor array in a stretched configuration and i) FEA result of the same. j) Photograph of fPCB that includes primary electronic components such as NFC SoC, low-dropout regulator (LDO), amplifier (AMP), and multiplexer (MUX). k) Block diagram involving four parts of the overall system: (1) battery-free, wireless device for measurement of pressure, shear, and temperature; (2) primary antenna and reader that transfer power to sensor array and communicate with sensor array; (3) laptop for monitoring data from wireless sensor in real-time and controlling pneumatic actuator; (4) pneumatic actuator that inflates or deflate air cells for relief of pressure and shear at skin interfaces.

© 2024 Wiley-VCH GmbH

16136829, 2024, 50, Downloaded from https://onlinelibrary.wiley.com/doi/10.1002/smll.202405493 by Korea University Medical Library, Wiley Online Library on [23/12/2024]. See the Terms and Conditions (https://onlinelibrary.wiley.com/terms-and-conditions) on Wiley Online Library for rules of use; OA articles are governed by the applicable Creative Commons License

difference between the two sensors was not significant. However, as the surface became softer (memory foam), the signal difference increased due to the stress concentration on the larger sensor. Thus, the signal difference between a gold standard (Pico-Press, Microlab, Italy) and the sensor would be minimal on softer surfaces with smaller sensor form factor.[14] In other words, a miniaturized sensor would guarantee more accurate data acquisition. To protect wireless sensor arrays from biofluids, such as sweat or liquid, top and bottom biocompatible polydimethylsiloxane (PDMS) layers were mechanically molded as shown in Figure S5 (Supporting Information) and then uncured PDMS bonded the edges of the top and bottom layers for encapsulation of the sensor arrays in Figure 1g and Figures S6 and S7 (Supporting Information). In regard to mechanical stimuli affecting wireless sensor arrays, strain distribution of the copper traces embedded in a flexible printed circuit board (fPCB) of 4 × 4 array does not exceed 0.26% when uniaxially stretched by a strain of 2.2% thanks to serpentine structural design as shown in the photograph and finite element analysis (FEA) results in Figure 1h,i. Moreover, the strain distribution of the copper traces was also examined under other mechanical stimuli, including bending and twisting in Figure S8 (Supporting Information).

Technological advances of the wireless platform in this study include integration of NFC SoC (RF430FRL152H, Texas Instruments, USA) with a multiplexer (MUX; TMUX1108, Texas Instruments, USA) and a low-dropout regulator (LDO; STLQ020C18R, STMicroelectronics, Switzerland) in Figure 1j and Figure S9 (Supporting Information). MUX provided NFC SoC with the capability to capture data from multiple sensors (i.e., 8:1 configuration), thereby achieving higher spatial densities of sensor array compared to the previous NFC-based wireless sensors (i.e., 1:1 configuration).[13,19–22] Besides, LDO regulated the antenna rectified voltage of NFC SoC from a voltage that varies ≈1.5 V to a fixed voltage of 1.8 V. Utilizing LDO as a voltage driver resulted in more uniform output voltage for the sensor array on the wireless platform compared to using the general-purpose input/output (GPIO) pin of NFC SoC as a voltage driver.[19,20,22]

Figure 1k presents a block diagram of the overall system as follows: 1) battery-free, wireless device for measurement of pressure, shear and temperature using electronic components such as LDO, MUX, and amplifier (AMP; INA333AIDRGT, Texas Instruments, USA); 2) primary antennas and antenna reader integrated with a clinical bed for power transfer and data communication with wireless sensor array; 3) PC to monitor mapping data from wireless sensor arrays in real-time and to control pneumatic actuator; 4) pneumatic actuator that inflates or deflates air cells for relief of pressure and shear at skin interfaces without intervention of manual handling.

2.2. Design Features and Performance Characteristics of a Miniaturized Pressure Sensor

Figure 2a presents exploded view of a miniaturized pressure sensor (4 × 4 × 1.1 mm^3) consisting of an fPCB substrate (polyimide (PI)/Cu/PI, 35/44/35 μm in thickness), a temperature sensor (NTC thermistor; NTCG064EF104FTBX, TDK Corporation, Japan) inside a rigid substrate (glass wafer, 500 μm in thickness), a strain gauge (PI/Au/PI, 3/0.03/75 μm in thickness), a soft block (PDMS, 200 μm in thickness), a rigid frame (silicon wafer, 250 μm in thickness), a membrane (PI, 75 μm in thickness), and a rigid pad (silicon wafer, 250 μm in thickness) (See Experimental Section and Figure S10 (Supporting Information) for a description of the fabrication process). In particular, incorporating rigid components, such as rigid substrate and rigid frame, into the assembly process of the pressure sensor provides insensitive properties against bending and shear forces as shown in Figure S11 (Supporting Information).[19,20,22] In addition, these rigid components do not cause any discomfort during wear, thanks to both PDMS encapsulation and a small form factor of 4 × 4 × 1.1 mm^3. The internal elastomeric soft block within the pressure sensor facilitates a conformal transmission of applied pressure to the top side of the strain gauge in Figure 2b. A lithographically designed strain gauge consists of a trilayer (i.e., Au pattern of 5 μm line width embedded inside PI film) in Figure 2c. In addition, Au pattern is positioned 35 μm away from the neutral axis of the strain gauge, unlike commercial strain gauges having a metal pattern on the neutral axis. One-sided Au pattern of the strain gauge stretches under applied pressure, resulting in tensile strain on Au pattern that increases the resistance of the strain gauge for pressure detection. Figure 2d presents FEA results of the pressure sensor under applied pressure of 100 kPa, illustrating a compressive strain of 0.3% on the top of the strain gauge and a tensile strain of 0.3% on the bottom of the strain gauge.

Cavity lengths (1–2.5 mm) of rigid substrate (glass wafer) tune the sensitivity of the pressure sensor based on beam deflection of the strain gauge from 3.2 × 10^{-5} kPa^{-1} within pressure range of 200 kPa–4.31 × 10^{-4} kPa^{-1} within pressure range of 15 kPa as shown in responses of the pressure sensor to a cycle of loading and unloading in Figure 2f, consistent with FEA results in Figure S12 (Supporting Information). The response of the sensor is expressed as $\Delta R/R_0$ (%), where ΔR is the difference between R and R_0, and R_0 represents the initial resistance of the strain gauge. Each pressure sensor, with different cavity lengths, exhibited high linearities (R^2) of 0.9997 (yellow; 1 mm), 0.9998 (black; 1.5 mm), 0.9997 (blue; 2.0 mm), and 0.9963 (red; 2.5 mm), as well as minimal hysteresis of 0.45%, 1.94%, 1.58%, and 1.86%, respectively. A cavity length dimension of 2 mm was chosen for high sensitivity of the pressure sensor within a pressure range of 30 kPa, a general pressure range for bedridden patients in hospitals.[3] Figure 2g presents the fractional change in resistance of the pressure sensor against four cyclic loadings of 7, 14, 21, and 30 kPa, respectively. Figure 2h illustrates the temperature-compensated response (black) of the pressure sensor in comparison to its original response (red; before compensation) using the temperature sensor (blue), across a temperature range of 20–40 °C (See Note S2, Supporting Information for additional information on temperature measurement and compensation). The compensated results indicate stable and consistent response of the pressure sensor under varying temperature conditions. Figure 2i presents both the original response of the pressure sensor (red; before compensation) under over 12 000 cyclic loadings (1 cycle s^{-1}) of 12.5 kPa, alongside the temperature sensor (blue) used for compensating the response of the pressure sensor (black; after compensation), exhibiting mechanical durability. Figure 2j demonstrates the stable response of the pressure sensor with negligible drift (<0.012%) under static loading of 30 kPa for more than 3 h, which is an important property for

© 2024 Wiley-VCH GmbH

16136829, 2024, 50, Downloaded from https://onlinelibrary.wiley.com/doi/10.1002/smll.202405493 by Korea University Medical Library, Wiley Online Library on [23/12/2024]. See the Terms and Conditions (https://onlinelibrary.wiley.com/terms-and-conditions) on Wiley Online Library for rules of use; OA articles are governed by the applicable Creative Commons License

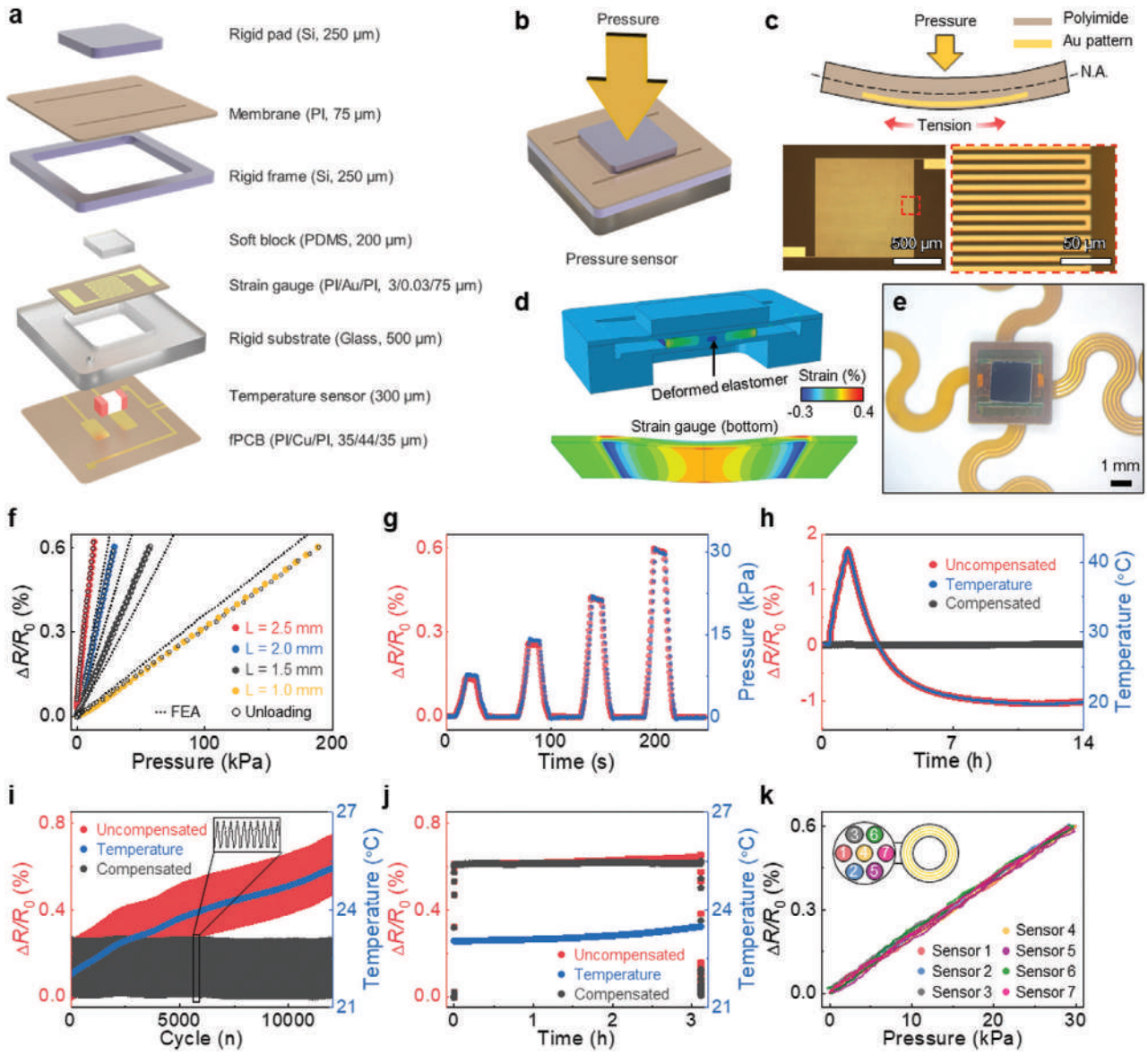


Figure 2. Design features, mechanism, and performance characteristics of a miniaturized pressure sensor. Schematic illustration of a) exploded view of the pressure sensor, b) the assembled pressure sensor under pressure applied on top, and c) a piezoresistive strain gauge (SG) under pressure. d) FEA results of the pressure sensor and SG under pressure of 100 kPa. e) Microscopic image of the miniaturized pressure sensor on fPCB. f) Fractional change in resistance of the pressure sensors with different cavity lengths (L) in rigid substrate (glass) according to applied pressure. g) Response of the pressure sensor against four cyclic loadings of 7, 14, 21, and 30 kPa, respectively. h) Response of the pressure sensor compensated using measured temperature (NTC thermistor) when temperature varies from 20 to 40 °C. i) Response of the pressure sensor under more than 10 000 cyclic loadings of 12.5 kPa. j) Response of the pressure sensor under static loading of 30 kPa. k) Fractional change in resistance of the seven pressure sensors under pressure from 0 to 30 kPa.

monitoring prolonged pressure at skin interfaces to prevent pressure injuries. In addition, Figure 2k presents the fine uniformity, i.e., sensor-to-sensor variations, in the sensitivity of seven pressure sensors by indicating a mean value of 2.02×10^{-4} kPa^{-1} and a standard deviation value of 3.25×10^{-6} kPa^{-1}.[24] Figure S13 (Supporting Information) exhibits average responses of seven pressure sensors with small deviations under sequential loadings, i.e., the fractional change in resistance of 0.169 ± 0.012 for 5 kPa, 0.329 ± 0.011 for 10 kPa, and 0.489 ± 0.008 for 15 kPa, respectively.

2.3. Design Features and Performance Characteristics of a Miniaturized Shear Sensor

Figure 3a,b presents a schematic illustration of a miniaturized shear sensor ($4 \times 4 \times 1.5$ mm^3) that includes an fPCB substrate (PI/Cu/PI, 35/44/35 μm in thickness), a PCB (FR-4, 400 μm in thickness), a rigid pillar (Ultem, $0.5 \times 0.5 \times 0.75$ mm^3), a 3D strain gauges (PI/Au/PI, 3/0.03/50 μm in thickness), an encapsulation layer (PDMS, 800 μm in thickness), and a rigid cover (silicon wafer, 250 μm in thickness) (See Experimental Section

© 2024 Wiley-VCH GmbH

16136829, 2024, 50, Downloaded from https://onlinelibrary.wiley.com/doi/10.1002/smll.202405493 by Korea University Medical Library, Wiley Online Library on [23/12/2024]. See the Terms and Conditions (https://onlinelibrary.wiley.com/terms-and-conditions) on Wiley Online Library for rules of use; OA articles are governed by the applicable Creative Commons License

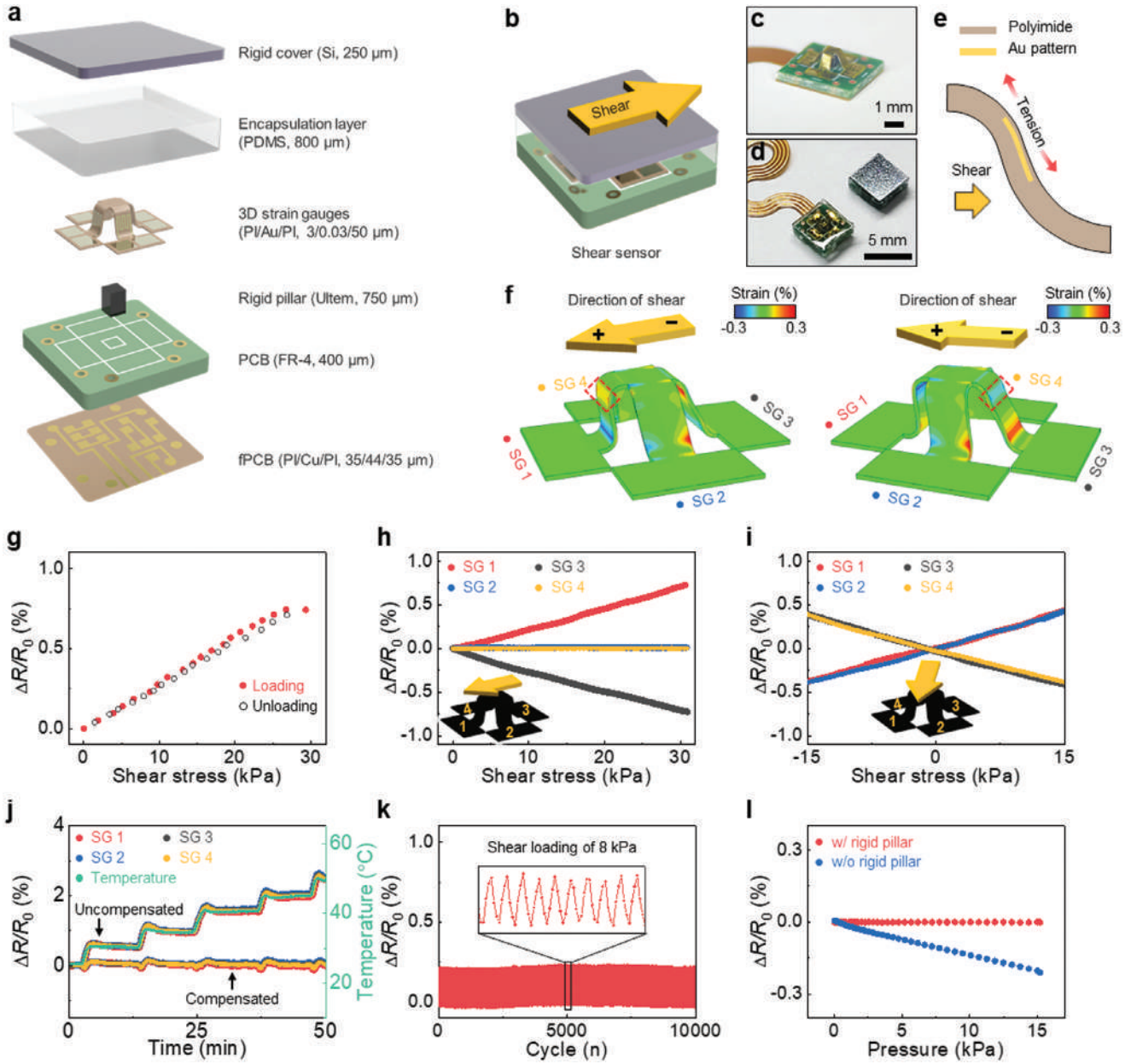


Figure 3. Design features, mechanism, and performance characteristics of a miniaturized shear sensor. Schematic illustration of a) exploded view of the shear sensor, b) the assembled shear sensor subjected to a shear applied on rigid cover. Photographs of the shear sensor c) before PDMS encapsulation and d) after PDMS encapsulation, followed by bonding of rigid cover. e) a partial strain gauge (SG) of the shear sensor subjected to shear. f) FEA results of the 3D strain gauges of the shear sensor subjected to a shear of 10 kPa. g) Fractional change in resistance of the shear sensor according to applied shear. Fractional change in resistance of four SGs of the shear sensors according to applied shear h) in the direction from SG 1 to SG 3 and i) in the direction from the midpoint between SG 4 and SG 3 to the midpoint between SG 1 and SG 2. j) Response of the four SGs of the shear sensor compensated using measured temperature (NTC) when temperature varies from 25 to 50 °C. k) Response of the shear sensor under 10 000 cyclic shear of 8 kPa. l) Response of the shear sensor with a rigid pillar according to applied pressure.

and Figure S10 (Supporting Information) for a description of the fabrication process). 3D strain gauges consist of four individual strain gauges (i.e., abbreviated as SG 1–SG 4) that enable the precise measurement of both the magnitude and direction of applied shear. Figure 3c presents a photograph of the shear sensor before PDMS encapsulation, clearly showing 3D strain gauges on a rigid pillar. Likewise, Figure 3d shows a photograph of the shear sensor after PDMS encapsulation (left) and after attaching the rigid cover (right) using a chemical bonding process at the interfaces of PDMS, silicon, and polyimide.[35] The rigid cover, strongly fixed on both top of the encapsulation layer and 3D strain gauges, transmits applied shear to the SGs, followed by tension occurring at outer top surface of the SG where Au pattern is intentionally placed (Figure 3e). FEA results on 3D strain gauges of the

© 2024 Wiley-VCH GmbH

16136829, 2024, 50, Downloaded from https://onlinelibrary.wiley.com/doi/10.1002/smll.202405493 by Korea University Medical Library, Wiley Online Library on [23/12/2024]. See the Terms and Conditions (https://onlinelibrary.wiley.com/terms-and-conditions) on Wiley Online Library for rules of use; OA articles are governed by the applicable Creative Commons License

shear sensor show 1) a tensile strain of 0.3% at outer top surface of SG 1 and 2) a compressive strain of 0.3% at outer top surface of SG 3 simultaneously when subjected to shear of 10 kPa in the direction from SG 3 to SG 1 in Figure 3f. In addition, the outer top surfaces of SG 2 and SG 4 exhibit negligible strain changes due to mismatch (i.e., orthogonal) between the direction of shear and the direction from SG 2 to SG 4. For convenience of analysis, we set the direction of shear acting on the shear sensor using positive (+) and negative (−) signs. For instance, increase in shear with positive value (>0 kPa) signifies increase in shear in the direction from SG 3 to SG 1, whereas decrease in shear with negative value (<0 kPa) indicates increase in shear in the direction from SG 1 to SG 3 in Figure 3f.

Figure 3g shows the fractional change in resistance of SG of the shear sensor during loading and unloading of shear of 30 kPa using a customized three-axis testing machine in Figure S14 (Supporting Information), exhibiting low hysteresis (2.4%), and high linearity (R^2 of 0.991). Figure 3h,i shows the responses of four SGs (SG 1–SG 4) of the shear sensor corresponding to the magnitude and direction of applied shear. In Figure 3h, the fractional change in resistance of SG 1 increases within a shear range of 30 kPa, while the fractional change in resistance of SG 3 decreases when shear is applied in the direction from SG 3 to SG 1. Interestingly, the fractional changes in resistance of SG 2 and SG 4, positioned orthogonally, are negligible. Figure S15 (Supporting Information) indicates the average responses of four SGs of the shear sensor with deviations under sequential shear loadings, i.e., the fractional change in resistance of 0.259 ± 0.024 for 10 kPa, 0.531 ± 0.058 for 20 kPa, and 0.731 ± 0.014 for 30 kPa, respectively. In addition, Figure 3i demonstrates the responses of four SGs with high linearity (R^2 of 0.998 ± 0.001) under resultant shear of 15 kPa, composed of two orthogonal shears of 15 × cos45° kPa, in the direction from the midpoint between SG 4 and SG 3 to the midpoint between SG 1 and SG 2. The responses of four SGs of the shear sensor (i.e., SG n = R_n; $\Delta R_n = R_n - R_0$, n = 1–4) determine the magnitude and direction of shear applied to the shear sensor using Equations (1) and (2) as follows, referring by the X and Y-axis coordinates in Figure S16a (Supporting Information).[27,31]

$$Shear\ stress_x\ (kPa) = \left(\Delta R_1 - \Delta R_3\right)/F \quad (1)$$

$$Shear\ stress_y\ (kPa) = \left(\Delta R_2 - \Delta R_4\right)/F \quad (2)$$

where F is a factor that changes according to the sensitivity of the shear sensor. F is 0.045 for a sensitivity of 2.8×10^{-4} kPa^{-1}. The linear superposition of the responses of four SGs can determine the magnitude and direction of shear (i.e., Shear $stress_x$ and Shear $stress_y$) using Equations (1) and (2) as shown in Figure S16b (Supporting Information), resulting from the responses of four SGs in Figure 3h. Figure 3j presents the temperature-compensated responses of four SGs of the shear sensor in response to temperature changes of 25–50 °C. The compensated results suggest that the temperature dependence of the shear sensor could be suppressed using the temperature data measured from NTC thermistor and calibration process, as described in Note S2 (Supporting Information). Figure S17a (Supporting Information) presents the average responses of four strain gauges of the shear sensor with deviations when temperature varies from 30 to 45 °C. Figure S17b (Supporting Information) shows responses of the integrated pressure and shear sensor, compensated using measured temperature (NTC), under sequential pressure loading of 10 kPa and shear loading of 15 kPa, followed by sequential pressure loading of 15 kPa and shear loading of 20 kPa, with simultaneous temperature variation from 43 to 57 °C. Figure 3k illustrates the long-term stability and mechanical durability of the shear sensor under 10 000 cyclic shear loading and unloading of 8 kPa. Figure 3l indicates a comparison result of the responses of the shear sensor with and without a rigid pillar under applied pressure of 15 kPa, exhibiting the insensitive property of the shear sensor with a rigid pillar against pressure. In addition, incorporating rigid components such as rigid pillars and PCB into the assembly process of the shear sensor provides insensitivity to bending and pressure, leading to mechanical decoupling of normal and shear forces when integrated with the pressure sensor, as supported by FEA results in Figure S18 (Supporting Information). Moreover, these rigid components with a small form factor of 4 × 4 × 1.5 mm^3 do not induce discomfort when attached to skin interfaces.

In summary, the rigid pillar effectively decouples pressure from shear forces, preventing any physical deformation and unwanted changes in the resistance of SGs due to pressure. This significant feature enables precise measurement of shear at the skin interfaces of patients.

2.4. Performance Characteristics of a Battery-Free, Wireless Device

Wheatstone bridge and AMP on the wireless device convert the fractional change in resistance of strain gauges, used in pressure and shear sensors, into an amplified change in voltage (See Note S3 and Figure S9, Supporting Information for additional information). The voltage outputs are converted into digital signals through an analog-to-digital converter (ADC) of NFC SoC, which is wirelessly transmitted for real-time monitoring based on ISO 15693 protocols at a resonant frequency of 13.56 MHz.

Figure 4a presents the change of ADC values measured from the wireless pressure sensor under cyclic loading and unloading of 30 kPa, exhibiting linearity (R^2 of 0.998) and negligible hysteresis of 1.43%. Figure 4b illustrates the change of ADC values of the wireless pressure sensor with a negligible drift under four cyclic loadings of 10, 17, 24, and 31 kPa. In Figure 4c, the wireless pressure sensor exhibited both a reliable, temperature-compensated response and durability under 5000 cyclic loading of 10 kPa, showing a minimal drift (See Note S4 and Figure S19a, Supporting Information for additional information on temperature measurement and compensation). Figure S19b (Supporting Information) presents the stable response of the wireless pressure sensor under static loading of 15 kPa for more than 1 h.

Figure 4d indicates the change of ADC values measured from four strain gauges (SG 1–SG 4) of the wireless shear sensor under cyclic shear loading and unloading of 30 kPa in the direction from SG 3 to SG 1. SG 1 and SG 3 exhibited linearities (R^2 of 0.981 and 0.973) with negligible hysteresis of 1.46% and 0.89%, respectively. Moreover, Figure 4e presents the response of the wireless shear sensor under cyclic shear loading and unloading of 20 kPa,

© 2024 Wiley-VCH GmbH

16136829, 2024, 50, Downloaded from https://onlinelibrary.wiley.com/doi/10.1002/smll.202405493 by Korea University Medical Library, Wiley Online Library on [23/12/2024]. See the Terms and Conditions (https://onlinelibrary.wiley.com/terms-and-conditions) on Wiley Online Library for rules of use; OA articles are governed by the applicable Creative Commons License

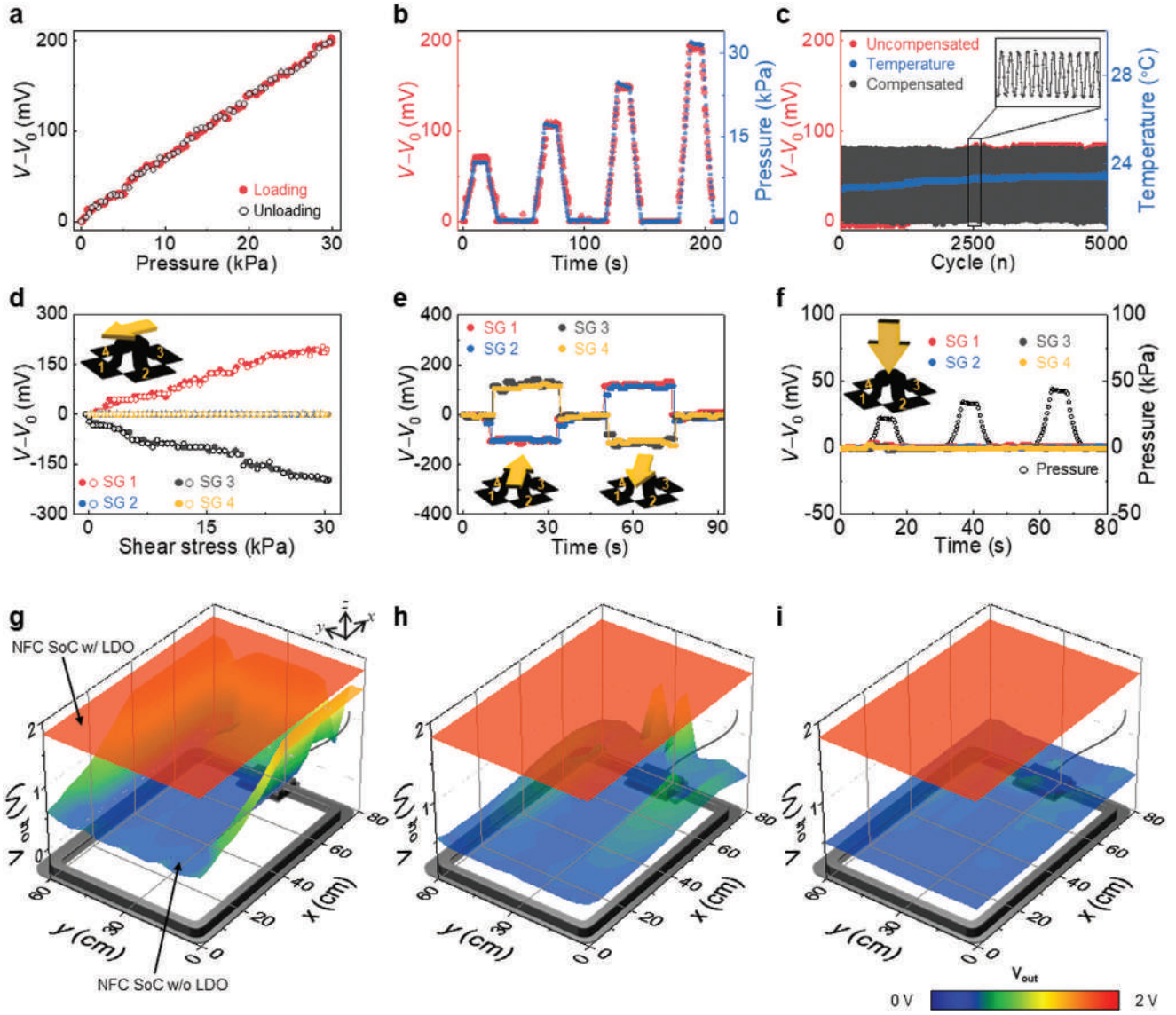


Figure 4. Performance characteristics of a battery-free, wireless device. a) Change of ADC values measured from the wireless pressure sensor according to applied pressure. b) Change of ADC values measured from the wireless pressure sensor against four cyclic loadings of 10, 17, 24, and 31 kPa, respectively. c) Change of ADC values measured from the wireless pressure sensor under 5000 cyclic loadings of 10 kPa. d) Change of ADC values measured from the wireless shear sensor according to applied shear in the direction from SG 1 to SG 3. e) Change of ADC values measured from the wireless shear sensor against cyclic shear of 20 kPa in the direction from the midpoint between SG 1 and SG 2 to the midpoint between SG 4 and SG 3. f) Change of ADC values measured from the wireless shear sensor with a rigid pillar according to applied pressure. Comparison of output voltage (V_{out}) obtained from NFC SoCs with and without low-dropout regulator (LDO) over a primary antenna ($62 \times 83.8 \times 2.6$ cm^3; ID ANT800/600, Feig Electronic, Germany) g) when the device is directly above antenna (z = 0 cm), h) when the device is 10 cm above antenna (z = 10 cm), and i) when the device is 20 cm above antenna (z = 20 cm).

applied in the direction from the midpoint between SG 1 and SG 2 to the midpoint between SG 4 and SG 3. Likewise, Figure S19c (Supporting Information) presents the change of ADC values measured from the wireless shear sensor under cyclic shear loading and unloading of 30 kPa in the direction from SG 1 to SG 3. The rigid pillar inside the wireless shear sensor provided the shear sensor with insensitive properties to normal forces and with sensitive properties to shear forces simultaneously, thereby achieving mechanical decoupling of normal and shear forces, as shown in Figure 4f.

In addition, Figure 4g–i provides comparison data regarding antenna rectified voltage of NFC SoC integrated with and without LDO over the primary antenna ($62 \times 83.8 \times 2.6$ cm^3; ID ANT800/600, Feig Electronic, Germany) at different xyz positions (e.g., x from 0 to 80 cm, y from 0 to 60 cm, and z from 0 to 20 cm). LDO regulated the antenna rectified voltage of NFC SoC from 1.5 to 1.8 V and stabilized the variation of the voltage according to xyz positions. The average value and standard deviation of the antenna rectified voltage at z = 0 cm were improved from 0.800 ± 0.416 V to 1.800 ± 0.001 V by integrating LDO into

© 2024 Wiley-VCH GmbH

16136829, 2024, 50, Downloaded from https://onlinelibrary.wiley.com/doi/10.1002/smll.202405493 by Korea University Medical Library, Wiley Online Library on [23/12/2024]. See the Terms and Conditions (https://onlinelibrary.wiley.com/terms-and-conditions) on Wiley Online Library for rules of use; OA articles are governed by the applicable Creative Commons License

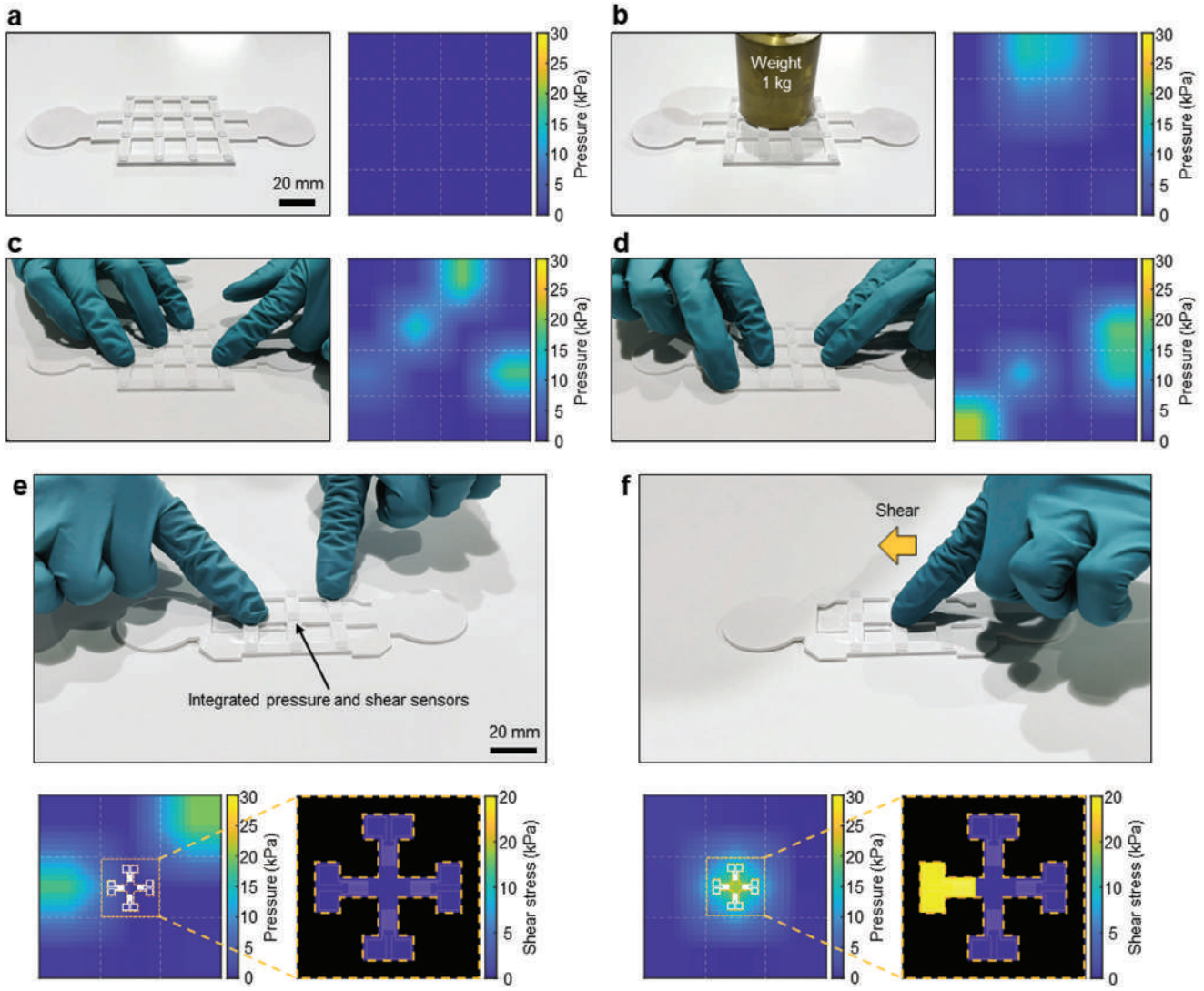


Figure 5. Demonstration of a battery-free, wireless device (4 × 4 and 3 × 3 arrays). Spatial mapping information obtained from 4 × 4 array a) when the sensor array is placed, b) when a 1 kg weight is placed on the sensor array, and c,d) when fingers apply pressure to the sensor array. Spatial mapping information obtained from 3 × 3 array e) when fingers apply pressure to the sensor array and f) when fingers apply shear to the sensor array.

NFC SoC in Figure 4g. Likewise, the average values and standard deviations were enhanced from 0.534 ± 0.115 V to 1.803 ± 0.001 (z = 10 cm) in Figure 4h and from 0.483 ± 0.025 V to 1.803 ± 0.001 (z = 20 cm) in Figure 4i, respectively. A constant supply of the regulated voltage of 1.8 V contributes to more reliable data acquisition of wireless sensor arrays at skin interfaces owing to stable operation.

2.5. Wireless Sensor Arrays for Real-Time Spatial Mapping of Pressure and Shear

Array configurations of multiple sensors provide more accurate and reliable information (i.e., spatial mapping data) compared to a single sensor. This improvement is achieved by enhancing spatial densities at locations of interest and alleviating the issue of mismatch in effective areas.[22–24] **Figure 5a** shows a 4 × 4 array consisting of 16 pressure sensors, 2 temperature sensors, and real-time spatial mapping information of pressure. (See Videos S1 and S2, Supporting Information for calibration process and real-time spatial mapping of 4 × 4 array, respectively). Figure 5b displays spatial mapping information of 4 × 4 array when a 1 kg weight was placed on the sensor array. Subsequently, Figure 5c,d presents spatial mapping information of 4 × 4 array when fingers apply pressure to the sensor array. Figure S21 (Supporting Information) offers continuously monitored mapping data of 4 × 4 array during the demonstration.

An interface between the pressure sensor and shear sensor was bonded using epoxy resin (1365868-6, Loctite, USA) at the central point of the 3 × 3 array as shown in Figures S7b,c and S10k,l (Supporting Information). Figure 5e shows a photograph of fingers applying pressure to 3 × 3 array, along with real-time spatial mapping information of pressure (bottom left) and shear (bottom right) below (See Videos S3 and S4, Supporting

© 2024 Wiley-VCH GmbH

16136829, 2024, 50, Downloaded from https://onlinelibrary.wiley.com/doi/10.1002/smll.202405493 by Korea University Medical Library, Wiley Online Library on [23/12/2024]. See the Terms and Conditions (https://onlinelibrary.wiley.com/terms-and-conditions) on Wiley Online Library for rules of use; OA articles are governed by the applicable Creative Commons License

Information for calibration process and real-time spatial mapping of 3 × 3 array, respectively). Figure 5f displays real-time spatial mapping information of pressure (22.9 kPa) and shear (19.3 kPa; left direction) as an index finger applies pressure and shear in the left direction. Figure S23 (Supporting Information) provides continuously monitored mapping data of 3 × 3 array during the demonstration.

2.6. Pneumatic Actuator Integrated with Clinical Bed for Inflation/Deflation of Air Cells

For relief of pressure and shear at specific locations of interest (i.e., patient-specific approach), a pneumatic actuator with twelve air cells, designed for full-body use, was customized and integrated with a clinical bed.

In sequence, **Figure 6a** presents two primary antennas for full-body coverage on the clinical bed, and Figure 6b shows wood frames protecting the primary antenna from physical impact. Subsequently, customized plastic frames were applied onto the wood frames to fix individual air cells (Figure S24, Supporting Information), and Figure 6c shows twelve air cells connected to syringes of the pneumatic actuator through the hose. Figure 6d,e presents photographs of the overall system, including 1) the clinical bed and air cells with hoses, 2) two primary antennas, a multiplexer (MUX) module, and an antenna reader, 3) an actuator platform consisting of a control box, a multi-axis linear actuator, and syringes, and 4) a laptop for real-time monitoring and actuation. Figure 6f shows a photograph of the multi-axis linear actuator that includes X and Y-axis step motors, four proximity sensors for position recognition, and a gripper for manipulating (e.g., pulling and pushing) a syringe with 600 mL capacity. Experimental Section and Figure S25 (Supporting Information) provide additional information on the inside of the control box for the operation of the pneumatic actuator. Video S5 (Supporting Information) demonstrates the sequential push and pull movement of the gripper on the multi-axis linear actuator from an initial point to a final point along the Y-axis of the linear actuator. Figure 6g,h shows the movement of the pneumatic actuator, pulling and pushing syringes back and forth using the gripper, thereby deflating and inflating the air cell with 2000 mL for relief of pressure and shear at skin interfaces as shown in Figure 6i,j. Video S6 (Supporting Information) presents the sequential movement of the gripper, pulling and pushing nine syringes to gradually increase or decrease the exhaust volume of air cells, as intended for the elaborate control of air cell volume. Video S7 (Supporting Information) presents the deflation and inflation of air cell in sequence, each by 1500 mL.

2.7. Evaluation of Pneumatic Actuator to Relieve Pressure and Shear at Skin Interfaces

To demonstrate the functionality and feasibility of the pneumatic actuator for bed-bound patients, our wireless device and two reference sensors, such as multi-axis loadcell (RFT60-HA01, Robotous, South Korea) and PicoPress (Microlab, Italy), were attached to the sacrum of a subject (30-year-old male, 75 kg, 175 cm) using a medical film dressing (1628 W, Tegaderm, USA) as shown in **Figures 7a,b** and S26 (Supporting Information). As the gripper pulls the syringe of the pneumatic actuator in 100 mL increments, the volume of air cell decreases until the syringe contains 1500 mL of air, exhibiting a simultaneous decreasing and converging trend in the responses of the three sensors (i.e., wireless device, multi-axis loadcell, and PicroPress) due to generation of space between the sacrum of the patient and the mattress in Figure 7c. The responses of the three sensors decrease as follows: 1) from 5.6 to 3.0 kPa for wireless device indicating a pressure reduction of 45.4%, 2) from 10.4 to 4.6 kPa for multi-axis loadcell indicating a pressure reduction of 56.0%, and 3) from 6.4 to 3.2 kPa for PicoPress indicating a pressure reduction of 50.0%, respectively. The reduced pressure value of ≈3 kPa achieved through the pneumatic actuator falls below the previously reported pressure value of 32 mmHg (i.e., arterial capillary pressure of 4.3 kPa) that impedes arterial blood flow over a prolonged period, leading to ischemia and necrosis of underlying tissue.[36,37] The relatively high response of multi-axis loadcell, compared to the responses of our wireless device and PicoPress, would be attributed to its bulky and rigid form factor, demonstrating the challenges in the practical use of the loadcell in biomedical applications. In contrast, the wireless device exhibited a response similar to PicoPress, known as a gold standard for measuring pressure at skin interfaces,[38–40] resulting from the thin and small form factor of wireless device. In this evaluation, shear did not occur at skin interfaces of the patient lying in a supine position on the clinical bed, as measured by multi-axis loadcell in Figure S27 (Supporting Information).

Figure 7d–h presents a real-time spatial mapping of pressure obtained from the patient lying in the clinical bed during the deflation of air cell for 1500 mL, acquired from a wireless sensor array. Figure 7d shows both a schematic anatomical illustration, providing information on locations of interest, and a photograph of 4 × 4 array attached to the sacrum. At the beginning of the experiment, the initial position (black dotted line) indicates the position of the belly before the deflation of air cell in Figure 7e. Figure 7f presents corresponding real-time spatial mapping information obtained from 4 × 4 array at the sacrum, indicating an average pressure value of 5.6 kPa ± 0.4 kPa. The red area in Figure 7g highlights the lowered position of the belly of patient after the deflation of air cell. Spatial mapping information also provides pressure distribution, with an average pressure value of 3.1 ± 0.4 kPa in Figure 7h. Video S8 and Figure S28 (Supporting Information) offer continuously monitored mapping data of 4 × 4 array at the sacrum of the patient lying in the clinical bed during the deflation of air cell.

To assess the functionality of the pneumatic actuator in relieving shear at the skin interfaces of the patient, the clinical bed was inclined at angles of 30°, 45°, and 60°, as shown in **Figure 8a–c**. Before using wireless device, a multi-axis loadcell (reference sensor) measured both pressure (Z-axis) of 7.7 ± 0.2 kPa and shear (X and Y-axis) of 4.1 ± 0.04 kPa at the sacrum of the patient lying in the inclined bed at an angle of 45° in Figure 8j.[3] After attaching a 3 × 3 array as shown in Figure 7b for measurement of pressure and shear at the sacrum of the patient lying in the inclined clinical bed, the air cell was deflated by 1500 mL. The inset in Figure 7b indicates SG 1–SG 4 of the shear sensor located at the center of the 3 × 3 array. Figure 8d–i presents real-time spatial mapping information of pressure and shear obtained from the

© 2024 Wiley-VCH GmbH

16136829, 2024, 50, Downloaded from https://onlinelibrary.wiley.com/doi/10.1002/smll.202405493 by Korea University Medical Library, Wiley Online Library on [23/12/2024]. See the Terms and Conditions (https://onlinelibrary.wiley.com/terms-and-conditions) on Wiley Online Library for rules of use; OA articles are governed by the applicable Creative Commons License



Figure 6. Pneumatic actuators integrated with a clinical bed. Photographs of a) two multiplexed primary antennas integrated with a clinical bed, b) wooden frame for stable power transfer and data communication of primary antennas, c) twelve air cells connected to syringes of pneumatic actuators via hoses, and d) thin mattress over air cells. d,e) Photographs of overall system that includes air cells of a clinical bed integrated with pneumatic actuators and a wireless platform. e) Photograph of monitoring and control system that includes laptop connected to NFC reader and multiplexer (MUX) for wireless power transfer and data communication, as well as connected to an actuator control box for movement of multi-axis (X and Y-axis) linear actuator. f) Photograph of multi-axis linear actuator that consists of X and Y-axis linear actuators, four proximity sensors for position recognition, and a gripper to grab a syringe. g–j) Photographs of the movement of pneumatic actuator system. Photograph of g) a moving gripper pulling syringes, inducing i) deflation of an air cell. Photograph of h) a moving gripper pushing syringes, inducing j) inflation of an air cell.

© 2024 Wiley-VCH GmbH

16136829, 2024, 50, Downloaded from https://onlinelibrary.wiley.com/doi/10.1002/smll.202405493 by Korea University Medical Library, Wiley Online Library on [23/12/2024]. See the Terms and Conditions (https://onlinelibrary.wiley.com/terms-and-conditions) on Wiley Online Library for rules of use; OA articles are governed by the applicable Creative Commons License

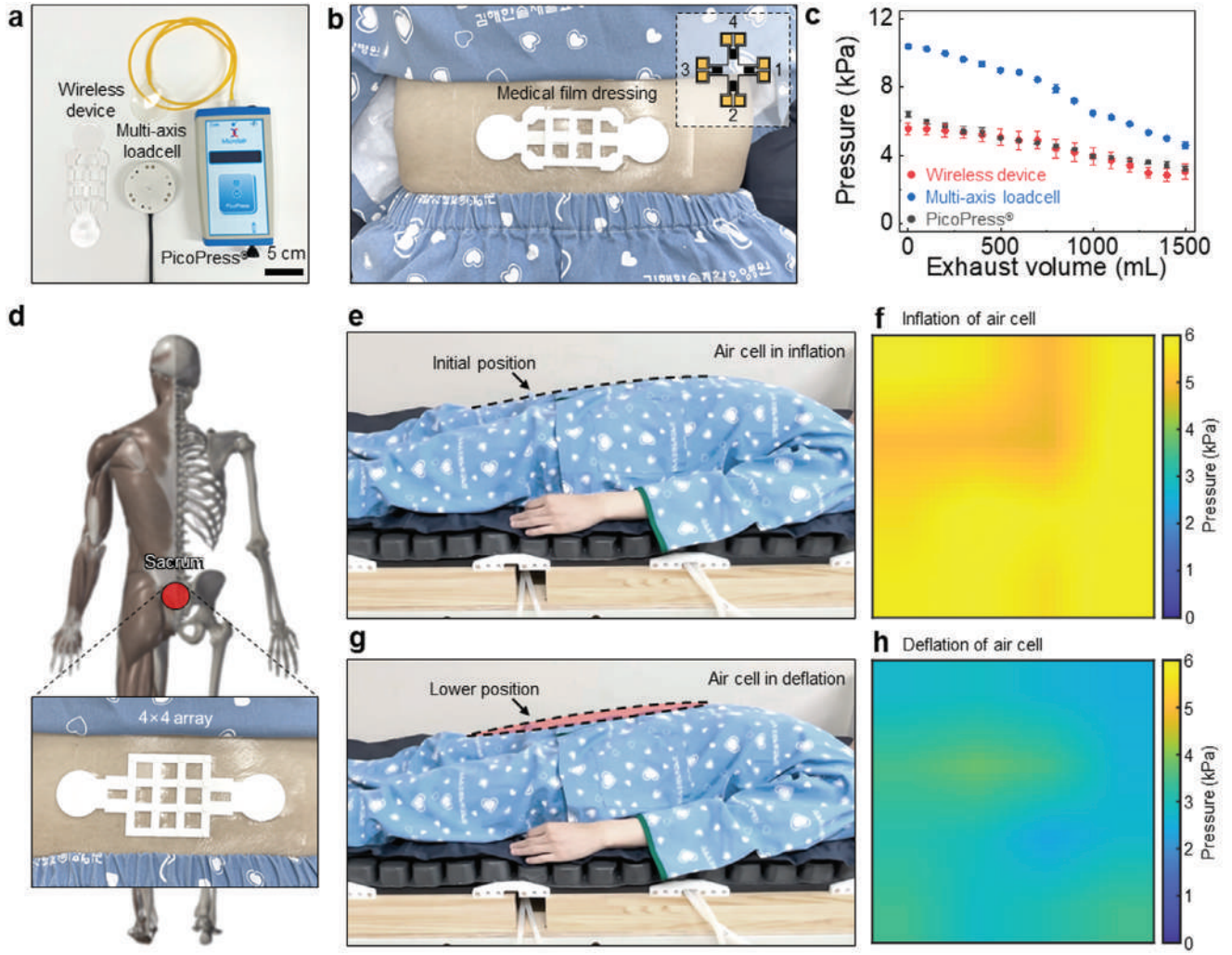


Figure 7. Preliminary test for evaluation of pneumatic actuator to relieve pressure at skin interfaces. Photographs of a) wireless device (3 × 3 array) and two reference sensors (e.g., multi-axis loadcell; Robotous, South Korea and PicoPress; Microlab, Italy) and b) wireless device attached to the sacrum of a subject (30-year-old male, 75 kg, 175 cm) using a medical film dressing (1628 W, TegadermTM, USA). c) Experimental results using three sensors attached to the sacrum of the subject lying in the bed while deflating air cell under the sacrum to relieve pressure at skin interfaces. d–h) Experimental results obtained from a 4 × 4 array attached to the sacrum of the subject lying in the bed utilizing pneumatic actuators to relieve the pressure at skin interfaces. d) Schematic anatomical diagram that shows a 4 × 4 array attached to the sacrum of the subject. e) Photograph of the subject lying in the bed and f) corresponding spatial mapping information for pressure obtained from a 4 × 4 array. g) Photograph of the subject lying in the bed while deflating the air cell under sacrum and h) corresponding spatial mapping information obtained from a 4 × 4 array.

patient lying in the inclined bed at angles of 30°, 45°, and 60°, respectively. Interestingly, pressure and shear values were high at a tilted angle of 30° before the deflation of air cell, exhibiting an average pressure value of 5.1 ± 0.2 kPa and maximum shear of 3.5 kPa, compared to values at an angle of 45° (an average pressure value of 4.1 ± 0.4 kPa and maximum shear of 3.1 kPa) and an angle of 60° (an average pressure value of 2.8 ± 0.4 kPa and maximum shear of 2.6 kPa), due to static friction applied to the shear sensor, which decreases as the inclined angle increases.[3] Figures S29–S31 (Supporting Information) provide continuously monitored mapping information of 3 × 3 array at the sacrum of the patient lying in the inclined bed at angles of 30°, 45°, and 60° during the deflation of air cell. The responses of 3 × 3 array to pressure and shear decreased and converged for three different tilted angles of the inclined bed as follows: 1) pressure reduced from 5.1 ± 0.2 to 1.1 ± 0.1 kPa, shear reduced from 3.3 to 0.1 kPa at a tilted angle of 30°; 2) pressure reduced from 4.1 ± 0.4 to 0.9 ± 0.3 kPa, shear reduced from 3.1 to 0.1 kPa at a tilted angle of 45°; and 3) pressure reduced from 2.8 ± 0.4 to 0.6 ± 0.3 kPa, shear reduced from 2.3 to 0.1 kPa at a tilted angle of 60° in Figure 8k,l. Likewise, the decrease in pressure and shear at skin interfaces resulted from the creation of volume between the sacrum and the mattress, as the air cell contracted. Video S9 (Supporting Information) presents continuously monitored mapping data of a 3 × 3 array at the sacrum of the patient lying in the inclined at angles of 30°, 45°, and 60° during the deflation of air cell.

To assess the skin condition after attaching the wireless device to skin interfaces for 3 h, three commercial sensors including skin analyzer for measurement of moisture and oil (Howskin IC-HSP001, INNOINSIGHT INC., South Korea), skin

© 2024 Wiley-VCH GmbH

16136829, 2024, 50, Downloaded from https://onlinelibrary.wiley.com/doi/10.1002/smll.202405493 by Korea University Medical Library, Wiley Online Library on [23/12/2024]. See the Terms and Conditions (https://onlinelibrary.wiley.com/terms-and-conditions) on Wiley Online Library for rules of use; OA articles are governed by the applicable Creative Commons License

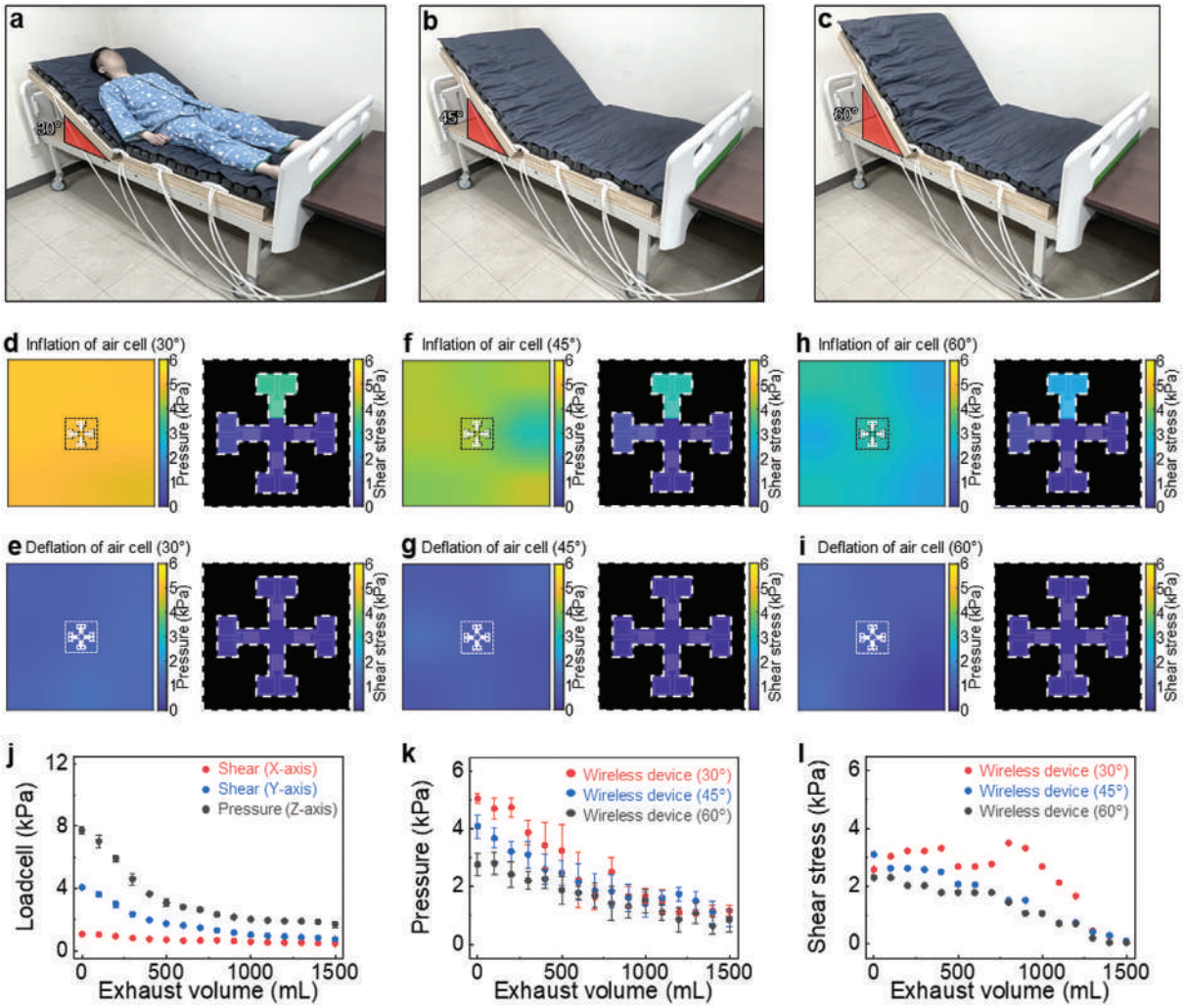


Figure 8. Preliminary test for evaluation of pneumatic actuator to relieve pressure and shear at skin interfaces. Photographs of the inclined bed at an angle of a) 30°, b) 45°, and c) 60°, respectively. Spatial mapping information for pressure and shear stress obtained from 3 × 3 array attached to the sacrum of the subject lying in the bed tilted at an angle of d and e) 30°, f,g) 45°, and h,i) 60°. Spatial mapping information for pressure and shear stress obtained from a 3 × 3 array attached to the sacrum of the subject lying in the bed tilted at an angle of e) 30°, g) 45°, and i) 60° while deflating the air cell under sacrum. j) Experimental results of multi-axis loadcell attached to the sacrum of the subject lying in the inclined bed at an angle of 45° while deflating air cell under the sacrum. k) Measurement of pressure using a wireless device attached to the sacrum of the subject lying in the inclined bed at angles of 30°, 45°, and 60° while deflating air cell under the sacrum. l) Measurement of shear using the wireless device attached to the sacrum of the subject lying in the inclined bed at angles of 30°, 45°, and 60°, respectively, according to the exhaust volume from the syringe.

colorimeter (DSM III ColorMeter, Timpac Healthcare, India), and infrared thermometer (SK-8300 SATO, Japan) were used every hour as shown in Figure S33a (Supporting Information). Figure S34 (Supporting Information) shows measurement results on skin conditions (e.g., moisture, oil, erythema index, and temperature) in three conditions: bare skin, skin after attaching a medical dressing, and skin after attaching the sensor with a medical dressing. No significant differences were observed among these three conditions. No irritation occurred after 3-h attachment, attributed to the use of biocompatible PDMS and a commercial medical dressing in Figure S33c,d (Supporting Information).

The experiments have demonstrated the functionality of the pneumatic actuator in relieving pressure and shear at location of interest without intervention of manual handling (i.e., repositioning) from medical staff. This approach can alleviate challenging issues associated with the shortage of nursing staff for patient repositioning,[41–44] reduce musculoskeletal injuries (i.e., occupational injuries) among caregivers,[45–49] and improve the quality of life by minimizing disruptions to sleep of patient.[12]

2.8. Validation Trial Involving Bed-Bound Patient Using Pneumatic Actuator

As individual systems, including 1) unit pressure, shear, temperature sensors, 2) wireless platform, and 3) pneumatic actuator, were evaluated, a validation trial using the overall system was conducted as follows. Wireless sensor arrays were attached to critical sites (highlighted in red) on the patient (30-year-old

© 2024 Wiley-VCH GmbH

16136829, 2024, 50, Downloaded from https://onlinelibrary.wiley.com/doi/10.1002/smll.202405493 by Korea University Medical Library, Wiley Online Library on [23/12/2024]. See the Terms and Conditions (https://onlinelibrary.wiley.com/terms-and-conditions) on Wiley Online Library for rules of use; OA articles are governed by the applicable Creative Commons License

male, 75 kg, 175 cm) lying in the clinical bed as follows: 4 × 4 arrays at the scapulae, 3 × 3 array at the sacrum, hexagonal arrays at the elbows, and pentagonal arrays at the heels (see **Figure 9a,b**; Figure S35, Supporting Information). Considering the curvatures of body parts, such as elbow, knee, and heel, hexagonal array and pentagonal array were used not only for higher spatial densities but also reliable data acquisition on curved surfaces in Figures S36 and S37 (See Note S5, Supporting Information for experimental results on hexagonal array applied to curved surfaces).[22–24]

Figure 9c presents real-time spatial mapping information of pressure and shear for the whole body prone to developing pressure injuries at the beginning of the validation trial, corresponding to a schematic anatomical illustration in Figure 9b. The average pressure and temperature values for each site were as follows: 1) 2.9 ± 0.5 kPa and 35.1 °C for the left scapula, 2) 2.4 ± 0.4 kPa and 35.9 °C for the right scapula, 3) 4.8 ± 0.3 kPa and 35.8 °C for the sacrum, 4) 2.4 ± 1.1 kPa and 34.6 °C for the left elbow, 5) 1.7 ± 0.5 kPa and 34.6 °C for the right elbow, 6) 1.9 ± 2.2 kPa and 34.9 °C for the left heel, and 7) 1.9 ± 2.6 kPa and 35.1 °C for the right heel, at t = 0 s in Figure 9c (Refer to Figures S38–S42, Supporting Information for continuously monitored mapping data of pressure, shear, and temperature for the entire body of the patient during the validation trial). The low-pressure range of 1.9–4.8 kPa (t = 0 s) would be attributed to the conformal contact between the body and the air mattress composed of twelve individual air cells.[50,51] The maximum shear value of 0.12 kPa at the sacrum (t of 27–62 s) during the validation trial was negligible, resulting from the patient being in a static supine position.[3] During the validation trial, air cells under left scapula, sacrum, and left heel of the bed-bound patient were sequentially deflated and inflated for 7 min to relieve pressure, as shown in Figure 9d,f,h. Figure 9e,g,i provides three significant mapping information of pressure after the deflation of air cell, among eight mapping information for the entire body in Figures S43–S45 (Supporting Information). As the air cell under left scapula deflated in Figure 9d, the average pressure value of the left scapula decreased by 62% (from 2.9 ± 0.5 to 1.1 ± 0.3 kPa), whereas the average pressure values of the right scapula and the sacrum increase by 54% (from 2.4 ± 0.4 to 3.7 ± 0.6 kPa) and 17% (from 4.8 ± 0.3 to 5.6 ± 0.3 kPa), respectively, due to a decreased effective area for body weight, as shown in Figure 9e. Figure S43 (Supporting Information) provides mapping information for the whole body during the deflation of air cell under the left scapula. After the air cell under the left scapula inflated again to its initial status, the air cell under the sacrum deflated, as illustrated in Figure 9f. The average pressure values of the left scapula and the right scapula increased by 24% (from 2.9 ± 0.5 to 3.6 ± 0.7 kPa) and 50% (from 2.4 ± 0.4 to 3.6 ± 0.7 kPa), respectively, while the average pressure value of the sacrum decreased by 33% (from 4.8 ± 0.3 to 3.2 ± 0.2 kPa) in Figure 9g. Likewise, Figure S44 (Supporting Information) offers mapping information for the entire body during the deflation of air cell under the sacrum. Lastly, after the air cell under the sacrum was reinflated, the air cell under the left heel deflated in Figure 9h. Although the average pressure value of the left heel slightly decreased by 5% (from 1.9 ± 2.2 to 1.9 ± 2.6 kPa), the maximum pressure value of the left heel decreased by 11% (from 5.1 to 4.5 kPa) in Figure 9i. Figure S45 (Supporting Information) also presents mapping information for the entire body during the deflation of air cell under the left heel. Figure 9j displays the continuously monitored average values of pressure and temperature obtained from the sensor arrays attached to critical sites of the patient in a static supine position during the deflation of the air cells. Video S10 (Supporting Information) presents real-time spatial mapping information obtained from sensor arrays during the validation trial.

In the context described, the smooth and minimal shift in body parts of the bed-bound patient using the pneumatic actuator has the potential to benefit individuals in static situations or circumstance associated with a high risk of pressure injuries (e.g., during sleep, surgery,[52] severe burns,[53] COVID-19,[54] etc.), where repositioning may be challenging. In addition, this battery-free, wireless platform that uses NFC technology for energy harvesting enables long-term continuous monitoring of risk factors at multiple locations of interest for biomedical applications as shown in Figure S46 (Supporting Information).

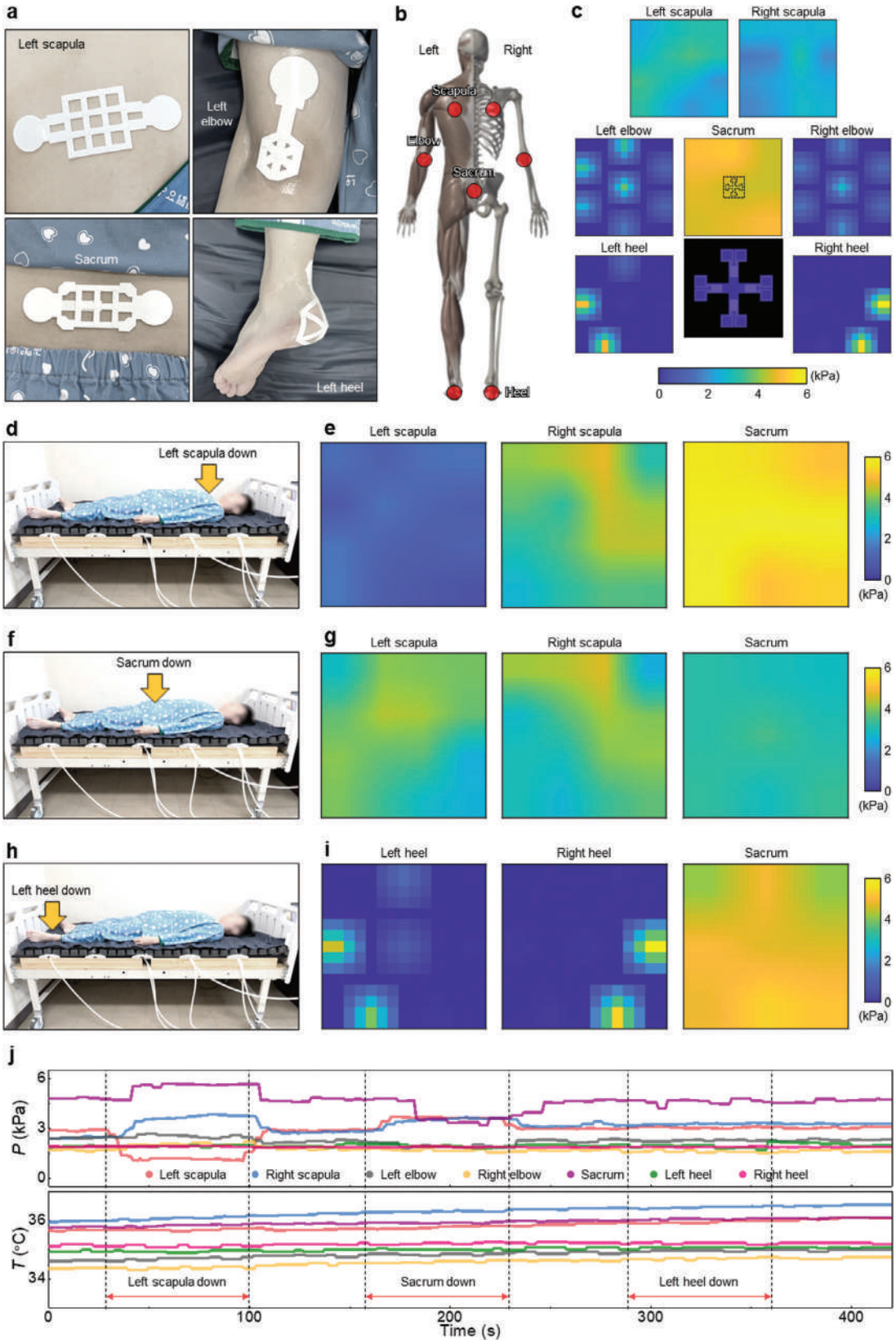
3. Discussion

The findings in this work underscore the critical role of advanced sensor technologies in the prevention of pressure injuries. The deployment of a battery-free, wireless multi-modal sensor arrays capable of measuring pressure, shear, and temperature simultaneously represents a significant leap forward in continuous monitoring of risk factors associated with formation of pressure injuries. In particular, 3D strain gauges in the shear sensor, along with the miniaturization and layering of pressure and temperature sensors, offers a new approach to capturing the complex interplay of forces at the skin interface. Moreover, the use of a customized pneumatic actuator in the validation trial emphasizes the importance of non-invasive, patient-friendly solutions in clinical settings, highlighting the potential to improve patient-reported outcomes without necessitating frequent repositioning that requires a workforce of medical staff. In addition, a novel combination of wireless sensor arrays and the pneumatic actuator improved the data reliability compared to the existing combination of mattress pressure mapping system and pneumatic actuator in terms of tracking critical sites.[55–58] This approach suggests a future research direction in personalized healthcare for pressure injury prevention through sensor data-based feedback control.

Future research should focus on refining the design and functionality of sensor platform to enhance its applicability across diverse healthcare settings as well as developing pneumatic actuator capable of optimal automatic control using datasets obtained from sensor platforms for measurement of diverse parameters (e.g., pressure, shear, temperature, and others). The exploration of advanced materials and sensor technologies may lead to even smaller, more efficient sensors with higher spatial densities, minimal interference, and maximal accuracy.[59,60] Additionally, establishing algorithms for the real-time analysis of sensor data along with machine/deep learning could provide predictive insights into the prevention of pressure injuries. Collaboration between engineers, clinicians, and patients is essential to ensure that these technological advancements align with clinical needs and patient comfort. In addition, extending the application of these sensors beyond the prevention of pressure injuries to other

© 2024 Wiley-VCH GmbH

16136829, 2024, 50, Downloaded from https://onlinelibrary.wiley.com/doi/10.1002/smll.202405493 by Korea University Medical Library, Wiley Online Library on [23/12/2024]. See the Terms and Conditions (https://onlinelibrary.wiley.com/terms-and-conditions) on Wiley Online Library for rules of use; OA articles are governed by the applicable Creative Commons License



© 2024 Wiley-VCH GmbH

16136829, 2024, 50, Downloaded from https://onlinelibrary.wiley.com/doi/10.1002/smll.202405493 by Korea University Medical Library, Wiley Online Library on [23/12/2024]. See the Terms and Conditions (https://onlinelibrary.wiley.com/terms-and-conditions) on Wiley Online Library for rules of use; OA articles are governed by the applicable Creative Commons License

areas of healthcare monitoring could pave the way toward customized care for patients.

4. Experimental Section

A Battery-Free, Wireless Platform: A flexible printed circuit board (fPCB; Pyralux AP8535 R, DuPont, USA) patterned by a UV laser cutter (ProtoLaser U4, LPFK Laser & Electronics AG, Germany) serves as a substrate for sensors including NTC thermistor (temperature sensor; NTCG064EF104FTBX, TDK Corporation, Japan) and electronic components such as NFC SoC (RF430FRL152H, Texas Instruments, USA), a multiplexer (MUX; TMUX1108, Texas Instruments, USA), a low-dropout (LDO; STLQ020C18R, STMicroelectronics, Switzerland) regulator, resistor (RC0201JR-07, Yageo, Taiwan) and capacitors (CL03B, Samsung Electro-Mechanics, South Korea) in Figures S47 and S48 (Supporting Information). The antenna rectified voltage of NFC SoC, regulated by LDO, is supplied as power for the pressure, shear, and temperature sensors. Analog signals obtained from the sensors are converted to digital signals using ADCs of NFC SoC for wireless data communications between the NFC SoC and an antenna reader (ID LRM2500, Feig Electronics, Germany), following ISO 15693 protocol of NFC at 13.56 MHz. Wheatstone bridge circuit for pressure and shear sensors and voltage divider circuit for temperature sensors support the conversion process from an analog signal to a digital signal as described in Notes S3 and S4 (Supporting Information).

Fabrication of a Strain Gauge: The fabrication process began with spin coating (1000 rpm for 30 s) of polyimide (PI) solution (PI-1388, VTEC, USA) on a silicon (Si) wafer (525 µm in thickness), followed by baking at 240 °C using a convection oven (See Figure S49a–f, Supporting Information for schematic illustrations regarding the process described). Subsequently, the spin coating process was performed four times in sequence to achieve a 75 µm thick PI film. Then, a negative photoresist (AZ nLof 2035, MicroChemicals GmbH, Germany) was spin-coated at 4000 rpm for 30 s, followed by baking at 110 °C for 1 min using a hot plate to obtain a thickness of 3 µm. After photolithography (UV irradiance of 72 mJ cm^{-2} for 8 s) using a patterned photo mask defined a resists pattern onto the Si wafer, a post-exposure baking (PEB) was conducted at 110 °C for 1 min using the hot plate. Subsequently, the Si wafer was immersed in a developer solution (AZ 300 MIF Developer, Omniscience, South Korea) for 2 min, and then rinsed with distilled (DI) water. To clean the residual photoresist, a plasma asher, operated at 50 W for 1 min, treated the patterned surface of the Si wafer before proceeding with an electron beam evaporation (E-beam) to improve adhesion properties. Chrome (Cr) and gold (Au) pattern layers, with thicknesses of 10 and 30 nm, respectively, were deposited using the E-beam. After deposition, the Si wafer was immersed in a solution (mr-Rem 700, micro resist technology GmbH, Germany) for 1 h for lift-off process, and then rinsed with isopropyl alcohol (IPA; J.T. Baker, USA) and DI water. The spin coating process using PI solution at 8000 rpm for 30 s on the Cr/Au pattern formed a thin, protective outer PI layer with a thickness of 3 µm, thereby completing the formation of a tri-layered strain gauge (PI/Au/PI, 3/0.03/75 µm in thickness) in Figure S49g,h (Supporting Information).

Fabrication of Miniaturized Pressure and Shear Sensors: The fabrication process of a miniaturized pressure sensor began with bonding a temperature sensor (NTC thermistor; NTCG064EF104FTBX, TDK Corporation, Japan) onto a fPCB (PI/Cu/PI, 35/44/35 µm in thickness) using a solder paste (SMDLTLFP10T5, Chip Quick, Canada) for electrical connection (Refer to Figure S10a–e, Supporting Information for schematic illustrations of the fabrication process for the pressure sensor). Subsequently, a rigid substrate (glass wafer; 4 × 4 × 0.5 mm^3), the strain gauge (PI/Au/PI; 3 × 1.5 × 0.078 mm^3), a soft block (polydimethylsiloxane (PDMS; Sylgard 184, Dow Inc., USA); 1 × 1 × 0.2 mm^3), a rigid frame (silicon wafer; 4 × 4 × 0.25 mm^3), a membrane (PI; 4 × 4 × 0.075 mm^3), and a rigid pad (silicon wafer; 2 × 2 × 0.25 mm^3) were prepared with the UV laser cutter and bonded in sequence using both the epoxy resin (1365868-6, Loctite, USA) and a silver epoxy (8331-14G, MG chemicals, Canada) for electrical connection.

The fabrication process of a miniaturized shear sensor began with bonding a PCB (FR-4; 4 × 4 × 0.4 mm^3) onto the fPCB using the epoxy resin (Refer to Figure S10f–j, Supporting Information for schematic illustrations of the fabrication process for the shear sensor). Likewise, a micromachined rigid pillar (Ultem, 0.5 × 0.5 × 0.75 mm^3) and 3D strain gauges (PI/Au/PI, 3/0.03/50 µm in thickness) were prepared with the UV laser cutter and bonded using both the epoxy resin and the silver epoxy. Then, a PDMS mixture of base and curing agent in a weight ratio of 10:1 was poured onto a 3D printed mold for PDMS encapsulation of the 3D strain gauges, followed by curing at room temperature overnight. The top surface of PDMS was chemically treated and bonded with a rigid cover (silicon wafer; 4 × 4 × 0.25 mm^3) as follows: 1) air plasma treatment at a power of 100 W for 10 min; 2) dropping a mixture solution of (3-Mercaptopropyl)trimethoxysilane (MPTMS; 175 617, Sigma–Aldrich, USA) and methanol (J.T. Baker, USA) in a volume ratio (v/v) of 1:100 onto the top surface of PDMS[35]; 3) rinsing the top surface of PDMS with DI water; 4) bonding the rigid cover onto top surface of PDMS using the epoxy resin.

Figure S10k,l (Supporting Information) indicates schematic illustrations of integrated pressure and shear sensors using the epoxy resin. Figure S48a,b (Supporting Information) presents the position where the pressure and shear sensors are integrated to complete the formation of a 3 × 3 array. PDMS top and bottom layers, utilized for encapsulating sensor arrays, were produced via a molding process using metal molds fabricated by a computer numerically controlled (CNC) milling machine (Promill Smart 3530, Protek, South Korea), as shown in Figures S5 and S7 (Supporting Information).

Finite Element Analysis: Abaqus (Dassault Systemes, France), a commercial finite element analysis (FEA) software, was used for FEA simulation of 1) fPCB under mechanical stimuli such as stretching, bending, and twisting, 2) pressure sensor, and 3) shear sensor. In sequence, fPCB, strain gauge of the pressure sensor, and 3D strain gauges of the shear sensor were modeled by S4R/S3 (S4R dominated), C3D8R, and C3D10 elements, respectively. The elastic modulus (E) and Poisson's ratio (υ) of the structures were E_{PI} = 2.5 GPa and υ_{PI} = 0.34 for polyimide; E_{Cu} = 130 GPa and υ_{Cu} = 0.34 for copper; E_{Glass} = 50 GPa and υ_{Glass} = 0.2 for glass; E_{Si} = 160 GPa and υ_{Si} = 0.27 for silicon; E_{PDMS} = 2.5 MPa and υ_{PDMS} = 0.5 for PDMS.

Characterization of Pressure, Shear, and Temperature Sensors: A UTM (AGS-X, Shimadzu, Japan) equipped with a load cell (SBL-1KN, Shimadzu, Japan) and a microactuator (MA-35, Physik Instrumente, Germany) equipped with a load cell (SM S-type load cell, Interface, USA) were used to apply cyclic loading and unloading to the pressure sensor. A customized, integrated three-axis testing machine consisting of multi-axis linear actuators and a three-axis load cell was used to apply the resultant load (i.e., combined pressure and shear) to the shear sensor in Figure S14 (Supporting Information). During loading, the fractional changes in resistance

Figure 9. Validation trial involving a subject (30-year-old male, 75 kg, 175 cm) confined to a bed using pneumatic actuators. a) Photographs of battery-free, wireless sensor arrays attached to critical locations prone to pressure injuries (e.g., 4 × 4 arrays at the scapulae, a 3 × 3 array at the sacrum, hexagonal arrays at the elbows, and pentagonal arrays at the heels) and b) corresponding schematic anatomical diagram. c) Spatial mapping information for pressure and shear obtained from sensor arrays attached to the subject lying in the bed. d) Photograph of the subject lying in the bed while deflating air cell under left scapula and e) corresponding spatial mapping information for pressure and shear stress obtained from sensor arrays attached to the subject lying in the bed. f) Photograph of the subject lying in the bed while deflating air cell under sacrum and g) corresponding spatial mapping information. h) Photograph of the subject lying in the bed while deflating air cell under left heel and i) corresponding spatial mapping information. j) Continuously monitored average values of pressure and temperature obtained from sensor arrays attached to critical locations of the subject during validation trial.

© 2024 Wiley-VCH GmbH

16136829, 2024, 50, Downloaded from https://onlinelibrary.wiley.com/doi/10.1002/smll.202405493 by Korea University Medical Library, Wiley Online Library on [23/12/2024]. See the Terms and Conditions (https://onlinelibrary.wiley.com/terms-and-conditions) on Wiley Online Library for rules of use; OA articles are governed by the applicable Creative Commons License

of the sensors were measured using a digital multimeter (USB 4065, National Instruments, USA) and a multimeter (Keithley 2700, Tektronix, USA) equipped with a multiplexer module (Keithley 7702, Tektronix, USA). An oven and a hotplate were used for varying temperature in the range of 20–50 °C.

Near Field Communication Protocol: A transmitter module (TRF7970A Evaluation Module, Texas Instruments, USA) connected with a laptop wirelessly embedded code into NFC SoC using a host software graphical user interface (GUI) at 13.56 MHz, in accordance with ISO 15693 protocol. Two primary antennas (ID ANT800/600, Feig Electronic, Germany), positioned over the clinical bed, connected to a multiplexer module (ID ANT.MUX.M4, Feig Electronic, Germany) and an antenna reader (ID LRM2500, Feig Electronics, Germany) enabled wireless power transfer and data communication using provided software (ISOStart 2018, Feig Electronics, Germany). The software set the RF power of the primary antenna to 8 W. In protocol mode as shown in Figure S50 (Supporting Information), ISOStart2018 software activates antenna 1 for 2000 ms and sequentially reads ADC values from four NFC SoCs, each endowed with a protocol tag, at intervals of 100 ms. Then, antenna 2 activates for 2000 ms for a sequential reading process of four NFC SoCs per 100 ms. The digital signals of NFC SoC, written in hexadecimal and received through the software, were converted to the change in voltage using Python for mapping information of pressure and shear in real-time. The baseline of the converted ADC value for each sensor was set as the ADC value of each sensor without any external stimuli (e.g., pressure and shear). When the external stimuli are applied, the ADC value increases or decreases from the baseline, thereby obtaining the change of ADC values from the wireless sensor array. In terms of power transfer, a vector network analyzer (VNA; TTR503A, Tektronix, USA) evaluated the power transfer efficiency (PTE; η) of the wireless sensing platform, indicating 74.6 ± 1.9%.[19,20,22]

Operation of Pneumatic Actuator: Inside the control box, there were 1) a power supply, 2) 2-axis motion controllers (PMC-2HSN-USB, Autonics Corp., South Korea), 3) X and Y-axis step motor drivers (MD2U-MD20, Autonics Corp., South Korea), and 4) a solenoid valve (SY7220-5LOZ-C10, SMC Korea corp., South Korea) connected with a compressor (OS100-E160-1H10, THOMAS, USA) that allowed the gripper to grip or release the syringe in Figure S25 (Supporting Information). Four proximity sensors (PR12-4DN, Autonics Corp., South Korea) were installed at each end of the X and Y- axis linear actuators, providing position information for the gripper. The use of proximity sensors to recognize the position of the gripper prevented over-actuation of the system. Based on the position information, the 2-axis motion controller operated the X and Y-axis step motor drivers and step motors (A16K-G268, Autonics Corp., South Korea), followed by the movement of gripper. All sequential procedures were carried out using a customized LabVIEW (National Instruments, USA) program on a laptop.

Mapping Process: Digital signals acquired from NFC SoC through ISOStart 2018 and Python were processed using MATLAB software (R2021a, MathWorks, USA) for mapping information of pressure and shear. In more detail, each data point from sensor arrays was processed using the "bilinear" method within "imresize" function in MATLAB. The process included halving the intervals ten times for continuous linear interpolation of the mapping information that provides intuitive, visual guidance to medical staff.

Validation Trial: This experiment was approved by the institutional review board (IRB) of the Korea Advanced Institute of Science and Technology (KAIST) (IRB no. KH2023-001). Before the experiment, the subject understood the study contents and signed the consent form in Figure S51 (Supporting Information). The subject was a 30-year-old male (175 cm, 75 kg), whose critical sites including scapula, elbows, sacrum, and heels were targeted by sensor arrays attached using a medical film dressing (1628 W, Tegaderm, USA). The pneumatic actuator integrated with the clinical bed inflated or deflated air cells while the subject was lying in the bed during the validation trial. The skin of the subject, where sensor arrays were attached, was evaluated after the validation trial using a skin analyzer (Howskin IC-HSP001, INNOINSIGHT INC., South Korea), a skin colorimeter (DSM III ColorMeter, Timpac Healthcare, India), and infrared thermometer (SK-8300 SATO, Japan) in Figure S33 (Supporting Information).

Statistical Analysis: The experimental results were expressed as mean ± standard deviation for sample sizes (n) more than four and analyzed using one-way ANOVA in MATLAB software (R2021a, MathWorks, USA), followed by Tukey's post-hoc test. $*p < 0.05$ and $**p < 0.01$ were considered statistically significant.

Supporting Information

Supporting Information is available from the Wiley Online Library or from the author.

Acknowledgements

H.H., S.C., and I.P. are supported by the Technology Innovation Program (00144157, Development of Heterogeneous Multi-Sensor Micro-System Platform) funded by the Ministry of Trade, Industry & Energy (MOTIE, Korea). Y.S.O. was supported by the National Research Foundation of Korea (NRF) grant funded by the Korean government (MSIT) (No. RS-2023-00212892).

Conflict of Interest

The authors declare no conflict of interest.

Author Contributions

H.H., H.P., and S.C. contributed equally to this work. H.H., H.P., S.C., Y.S.O., M.J., and I.P. led the development of the concepts, designed the experiments, and interpreted the results. H.H. led the experimental work with support from S.U.L., J.C., J.H.H., J.P., Y.J., H.K., J.A. And Y.J.K., H.H., and I.P. wrote the paper.

Data Availability Statement

All data needed to evaluate the conclusions in the paper are present in the paper and/or the Supplementary Materials. Additional data related to this paper may be requested from the corresponding authors.

Keywords

battery-free, pneumatic actuator, pressure and shear sensors, pressure injuries, wireless sensor array

Received: July 3, 2024
Revised: July 17, 2024
Published online: August 1, 2024

[1] B. Dorner, M. E. Posthauer, D. Thomas, N. P. U. A. Panel, *Adv. Skin Wound Care* **2015**, *28*, 175.
[2] A. Gorgey, D. Gater, *Top Spinal Cord Inj Rehabil* **2007**, *12*, 1.
[3] M. Mimura, T. Ohura, M. Takahashi, R. Kajiwara, N. Ohura Jr., *Wound Repair Regener.* **2009**, *17*, 789.
[4] V. V. Broderick, L. J. Cowan, *J Dermatol Skin Sci* **2021**, *3*, 2.
[5] J. S. Akins, P. E. Karg, D. M. Brienza, *J Rehabil Res Dev* **2011**, *48*, 225.

© 2024 Wiley-VCH GmbH

16136829, 2024, 50, Downloaded from https://onlinelibrary.wiley.com/doi/10.1002/smll.202405493 by Korea University Medical Library, Wiley Online Library on [23/12/2024]. See the Terms and Conditions (https://onlinelibrary.wiley.com/terms-and-conditions) on Wiley Online Library for rules of use; OA articles are governed by the applicable Creative Commons License

[6] G. Nakagami, H. Sanada, C. Konya, A. Kitagawa, E. Tadaka, K. Tabata, *J. Wound Ostomy Continence* **2006**, *33*, 267.
[7] M. Nagao, T. Ohura, M. Takahashi, M. Osawa, *Plast Reconstr Surg* **2023**, *2*, 9.
[8] C. Lachenbruch, Y.-T. Tzen, D. M. Brienza, P. E. Karg, P. A. Lachenbruch, *Ostomy Wound Manage* **2013**, *59*, 25.
[9] J. Y. Kokate, K. J. Leland, A. M. Held, G. L. Hansen, G. L. Kveen, B. A. Johnson, M. S. Wilke, E. M. Sparrow, P. A. Iaizzo, *Arch. Phys. Med. Rehabil.* **1995**, *76*, 666.
[10] J. Cox, *Am. J. Critical Care* **2011**, *20*, 364.
[11] S. Smith, A. Snyder, L. F. McMahon, L. Petersen, J. Meddings, *Health Aff.* **2018**, *37*, 1787.
[12] B. M. Gillespie, R. M. Walker, S. L. Latimer, L. Thalib, J. A. Whitty, E. McInnes, W. P. Chaboyer, *Cochrane Database Syst. Rev.* **2020**, *2020*, 103976.
[13] S. Han, J. Kim, S. M. Won, Y. Ma, D. Kang, Z. Xie, K.-T. Lee, H. U. Chung, A. Banks, S. Min, S. Y. Heo, C. R. Davies, J. W. Lee, C.-H. Lee, B. H. Kim, K. Li, Y. Zhou, C. Wei, X. Feng, Y. Huang, J. A. Rogers, *Sci. Transl. Med.* **2018**, *10*, eaan4950.
[14] Y. Park, K. Kwon, S. S. Kwak, D. S. Yang, J. W. Kwak, H. Luan, T. S. Chung, K. S. Chun, J. U. Kim, H. Jang, H. Ryu, H. Jeong, S. M. Won, Y. J. Kang, M. Zhang, D. Pontes, B. R. Kampmeier, S. H. Seo, J. Zhao, I. Jung, Y. Huang, S. Xu, J. A. Rogers, *Sci. Adv.* **2024**, *6*, eabe1655.
[15] C. K. Franz, N. K. Murthy, G. R. Malik, J. W. Kwak, D. D'Andrea, A. R. Wolfe, E. Farr, M. A. Stearns, S. Deshmukh, J. O. Tavee, F. Sun, K. N. Swong, L. Rydberg, R. J. Cotton, L. F. Wolfe, J. M. Walter, J. M. Coleman, J. A. Rogers, *J Neuroeng Rehabil* **2022**, *19*, 108.
[16] N. Mehmood, A. Hariz, S. Templeton, N. H. Voelcker, *Biomed. Eng. Online* **2015**, *14*, 17.
[17] J. Kim, J. Park, Y. G. Park, E. Cha, M. Ku, H. S. An, K. P. Lee, M. Il Huh, J. Kim, T. S. Kim, D. W. Kim, H. K. Kim, J. U. Park, *Nat. Biomed. Eng.* **2021**, *5*, 772.
[18] J. Jang, J. Kim, H. Shin, Y.-G. Park, B. Jun Joo, H. Seo, J. Won, D. Woo Kim, C. Young Lee, H. Kyun Kim, J.-U. Park, Smart Contact Lens and Transparent Heat Patch for Remote Monitoring and Therapy of Chronic Ocular Surface Inflammation Using Mobiles **2021**.
[19] S. Cho, H. Han, H. Park, S. U. Lee, J. H. Kim, S. W. Jeon, M. Wang, R. Avila, Z. Xi, K. Ko, M. Park, J. Lee, M. Choi, J. S. Lee, W. G. Min, B. J. Lee, S. Lee, J. Choi, J. Gu, J. Park, M. S. Kim, J. Ahn, O. Gul, C. Han, G. Lee, S. Kim, K. Kim, J. Kim, C. M. Kang, J. Koo, et al., *npj Flexible Electron.* **2023**, *7*, 8.
[20] Y. S. Oh, J.-H. Kim, Z. Xie, S. Cho, H. Han, S. W. Jeon, M. Park, M. Namkoong, R. Avila, Z. Song, S.-U. Lee, K. Ko, J. Lee, J.-S. Lee, W. G. Min, B.-J. Lee, M. Choi, H. U. Chung, J. Kim, M. Han, J. Koo, Y. S. Choi, S. S. Kwak, S. B. Kim, J. Kim, J. Choi, C.-M. Kang, J. U. Kim, K. Kwon, S. M. Won, et al., *Nat. Commun.* **2021**, *12*, 5008.
[21] J. W. Kwak, M. Han, Z. Xie, H. U. Chung, J. Y. Lee, R. Avila, J. Yohay, X. Chen, C. Liang, M. Patel, *Sci. Transl. Med.* **2020**, *12*, eabc4327.
[22] H. Han, Y. S. Oh, S. Cho, H. Park, S.-U. Lee, K. Ko, J.-M. Park, J. Choi, J.-H. Ha, C. Han, Z. Zhao, Z. Liu, Z. Xie, J.-S. Lee, W. G. Min, B.-J. Lee, J. Koo, D. Y. Choi, M. Je, J.-Y. Sun, I. Park, *Small* **2023**, *19*, 2205048.
[23] M. Kang, H. Jeong, S.-W. Park, J. Hong, H. Lee, Y. Chae, S. Yang, J.-H. Ahn, *Sci. Adv.* **2024**, *8*, eabm6693.
[24] M. Han, L. Chen, K. Aras, C. Liang, X. Chen, H. Zhao, K. Li, N. R. Faye, B. Sun, J.-H. Kim, W. Bai, Q. Yang, Y. Ma, W. Lu, E. Song, J. M. Baek, Y. Lee, C. Liu, J. B. Model, G. Yang, R. Ghaffari, Y. Huang, I. R. Efimov, J. A. Rogers, *Nat. Biomed. Eng.* **2020**, *4*, 997.
[25] E. Russell-Goldman, G. F. Murphy, *Am J Pathol* **2020**, *190*, 1356.
[26] Y. Yan, Z. Hu, Z. Yang, W. Yuan, C. Song, J. Pan, Y. Shen, *Sci Robot* **2021**, *6*, eabc8801.
[27] S. M. Won, H. Wang, B. H. Kim, K. Lee, H. Jang, K. Kwon, M. Han, K. E. Crawford, H. Li, Y. Lee, X. Yuan, S. B. Kim, Y. S. Oh, W. J. Jang, J. Y. Lee, S. Han, J. Kim, X. Wang, Z. Xie, Y. Zhang, Y. Huang, J. A. Rogers, *ACS Nano* **2019**, *13*, 10972.
[28] A. Tariq, A. Behravesh, G. Rizvi, *Eng. Res. Express* **2023**, *5*, 032002.
[29] D. Choi, S. Jang, J. S. Kim, H.-J. Kim, D. H. Kim, J.-Y. Kwon, *Adv. Mater. Technol.* **2019**, *4*, 1800284.
[30] J. Ham, T. M. Huh, J. Kim, J.-O. Kim, S. Park, M. R. Cutkosky, Z. Bao, *Adv. Mater. Technol.* **2023**, *8*, 2200903.
[31] C. Hou, K. Wang, F. Wang, H. Li, L. Lou, S. Zhang, Y. Gu, H. Liu, T. Chen, L. Sun, *Adv. Funct. Mater.* **2023**, *33*, 2302812.
[32] J. Park, J. Kim, J. Hong, H. Lee, Y. Lee, S. Cho, S.-W. Kim, J. J. Kim, S. Y. Kim, H. Ko, *NPG Asia Mater* **2018**, *10*, 163.
[33] A. Gefen, P. Alves, G. Ciprandi, F. Coyer, C. T. Milne, K. Ousey, N. Ohura, N. Waters, P. Worsley, *J Wound Care* **2020**, *29*, S1.
[34] J. Y. Kim, Y. J. Lee, Korean Association of Wound Ostomy Continence Nurses, *Int. Wound J.* **2019**, *16*, 51.
[35] M. V. Hoang, H.-J. Chung, A. L. Elias, *J. Micromech. Microeng.* **2016**, *26*, 105019.
[36] A. Gefen, *Nurs. Stand.* **2009**, *23*, 64.
[37] S. Bhattacharya, R. K. Mishra, *Indian Journal of Plastic Surgery* **2015**, *48*, 4.
[38] H. Partsch, G. Mosti, *Int Angiol* **2010**, *29*, 426.
[39] C. R. Lattimer, M. Azzam, E. Kalodiki, G. C. Makris, G. Geroulakos, *J Vasc Surg Venous Lymphat Disord* **2013**, *58*, 158.
[40] S. Y. Lee, Y. S. Cho, S. Y. Joo, C. H. Seo, *Burns* **2021**, *47*, 1621.
[41] J. Qaddumi, A. Khawaldeh, *BMC Nurs.* **2014**, *13*, 6.
[42] J.-B. Combes, R. F. Elliott, D. Skåtun, *Appl. Econ.* **2018**, *50*, 6547.
[43] K. Zarea, R. Negarandeh, N. Dehghan-Nayeri, M. Rezaei-Adaryani, *Nurs Health Sci.* **2009**, *11*, 326.
[44] U. Källman, B.-O. Suserud, *Scand J Caring Sci* **2009**, *23*, 334.
[45] A. R. Darragh, C. M. Sommerich, S. A. Lavender, K. J. Tanner, K. Vogel, M. Campo, *J Appl Gerontol* **2013**, *34*, 734.
[46] A. Karahan, S. Kav, A. Abbasoglu, N. Dogan, *J Adv Nurs* **2009**, *65*, 516.
[47] I. Kuorinka, B. Jonsson, A. Kilbom, H. Vinterberg, F. Biering-Sørensen, G. Andersson, K. Jørgensen, *Appl Ergon.* **1987**, *18*, 233.
[48] C. Weiner, D. Alperovitch-Najenson, J. Ribak, L. Kalichman, *Workplace Health Saf.* **2015**, *63*, 226.
[49] L. A. Pompeii, H. J. Lipscomb, A. L. Schoenfisch, J. M. Dement, *Am. J. Ind. Med.* **2009**, *52*, 571.
[50] S. E. Sonenblum, T. E. Vonk, T. W. Janssen, S. H. Sprigle, *Arch. Phys. Med. Rehabil.* **2014**, *95*, 1350.
[51] A. Gil-Agudo, A. De la Peña-González, A. Del Ama-Espinosa, E. Pérez-Rizo, E. Díaz-Domínguez, A. Sánchez-Ramos, *Clin. Biomech.* **2009**, *24*, 558.
[52] O. Ezeamuzie, V. Darian, U. Katiyar, A. Siddiqui, *Perioper Care Oper Room Manag* **2019**, *17*, 100080.
[53] D. E. Fritsch, T. L. Coffee, C. J. Yowler, *J. Burn Care Rehabil.* **2001**, *22*, 293.
[54] M. Barakat-Johnson, R. Carey, K. Coleman, K. Counter, K. Hocking, T. Leong, A. Levido, F. Coyer, *Wound Practice and Research* **2020**, *28*, 50.
[55] S. Arias, E. Cardiel, L. Garay, B. Tovar, M. Pla, P. Rogeli, in *2013 35th Annual Int. Conf. of the IEEE Engineering in Medicine and Biology Society (EMBC)*, IEEE, xx xx **2013**, pp. 4751–4754.
[56] K.-H. Lee, Y.-E. Kwon, H. Lee, Y. Lee, J. Seo, O. Kwon, S.-W. Kang, D. Lee, *Sensors* **2019**, *19*, 3862.
[57] D. Mannella, M. Bellusci, F. Graziani, C. Ferraresi, G. G. Muscolo, *Proc Inst Mech Eng H* **2022**, *236*, 592.
[58] J. Zhou, W. Li, H. Hu, *Comput Intell Neurosci* **2022**, *2022*, 4895038.
[59] J. W. Kwak, M. Han, Z. Xie, H. U. Chung, J. Y. Lee, R. Avila, J. Yohay, X. Chen, C. Liang, M. Patel, I. Jung, J. Kim, M. Namkoong, K. Kwon, X. Guo, C. Ogle, D. Grande, D. Ryu, D. H. Kim, S. Madhvapathy, C. Liu, D. S. Yang, Y. Park, R. Caldwell, A. Banks, S. Xu, Y. Huang, S. Fatone, J. A. Rogers, *Sci. Transl. Med.* **2020**, *12*, eabc4327.
[60] Y. Park, H. Luan, K. Kwon, T. S. Chung, S. Oh, J.-Y. Yoo, G. Chung, J. Kim, S. Kim, S. S. Kwak, J. Choi, H.-P. Phan, S. Yoo, H. Jeong, J. Shin, S. M. Won, H.-J. Yoon, Y. H. Jung, J. A. Rogers, *npj Flexible Electron.* **2024**, *8*, 6.

© 2024 Wiley-VCH GmbH

16136829, 2024, 50, Downloaded from https://onlinelibrary.wiley.com/doi/10.1002/smll.202405493 by Korea University Medical Library, Wiley Online Library on [23/12/2024]. See the Terms and Conditions (https://onlinelibrary.wiley.com/terms-and-conditions) on Wiley Online Library for rules of use; OA articles are governed by the applicable Creative Commons License